Electronic Supplementary Material (ESI) for ChemComm.

Elongation of Magnetic Relaxation Times in a Single−Molecule Magnet through Intermetallic Interactions: Clamshell−Type Dinuclear Terbium(III)−Phthalocynaninato Quadruple−Decker Complex

Yoji Horii,[a] Keiichi Katoh,[a*] Brian. K. Breedlove[a] and Masahiro Yamashita[a,b,c*]

[a] Department of Chemistry, Graduate School of Science, Tohoku University, 6−3, Aramaki−Aza−Aoba, Aoba−ku, Sendai 980−8578, Japan.

[b] WPI Research Center, Advanced Institute for Materials Research, Tohoku Universi−ty, 2−1−1 Katahira, Aoba−ku, Sendai 980−8577, Japan.

[c] School of Materials Science and Engineering, Nankai University, Tianjin 300350, China

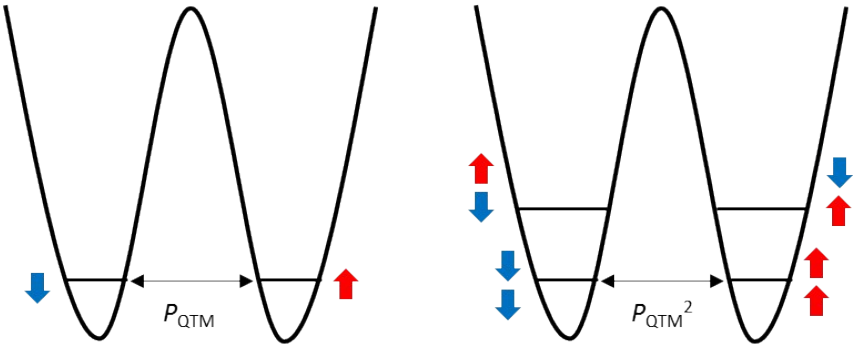

Figure S1. Changes in QTM possibility in the double−well potentials of isolated SMM and coupled SMMs. If the possibility for QTM in an isolated SMM is expressed as P_{QTM}, the QTM in the coupled SMMs is expressed as P_{QTM}^2 because simultaneous two spin reversal is required in the latter case. Because P_{QTM}^2 is smaller than P_{QTM}, QTM is effectively suppressed in coupled SMMs.

Synthesis

Reagents were purchased and used without further purification. 1,2,4−Trichlorobenzene were purchased from Aldrich. Other reagents and the solvents were purchased from Wako. Clamshell type phthalocyanine[1], phenoxthiin hexachloroantimonate ($SbCl_6 \cdot Ox$)[2] and $TbPc(CH_3CO_2)$[3] were synthesized according to the literature methods.

Clamshell type quadruple-decker complex [Tb_2]

In an N_2 atmosphere, clamshell Pc (74 mg, 0.049 mmol), $TbPc(CH_3CO_2)$ (70 mg, 0.096 mmol) were mixed with 3 mL of 1,2,4-trichlorobenzene, 1 mL of 1-hexanol and 0.5 mL of 1,8-diazabicyclo[5.4.0]undec-7-ene (DBU). The mixture was refluxed for 2 h in an N_2 atmosphere. Solvent was evaporated in the vacuum condition. The residue was purified by using chromatography on silica gel (Wakogel c-200) with $CHCl_3$ as the eluent. The main green band was collected, and the solvent was evaporated. Further purification of that band by using chromatography on silica gel (Wakogel c-400HG) with $CHCl_3$ as the eluent afforded pure [Tb_2]. 42 mg (16%) CHN elemental analysis calcd (%) for $C_{160}H_{118}N_{32}O_2Tb_2$: C 67.70, H 4.19, N 15.79; found: C 67.41, H 4.52, N 15.64. ESI−MS; 1419.37 $[M]^{2+}$ (calcd 1419.94)

Cadmium(II)-inserted quadruple-decker complex [Tb_2Cd]

[Tb_2] (10 mg, 3.5 μmol) and $Cd(CH_3CO_2)_2 \cdot 2H_2O$ (10 mg, 38 μmol) were mixed in 1 mL of 1-hexanol and 0.5 mL of 1,2,4-TCB for 30 min in a N_2 atmosphere. The solvent was removed in the reduced pressure, and the residue was purified by using chromatography over silica gel column chromatography (Wakogel c-400HG). The deep blue fraction was collected and recrystallized from CH_2Cl_2/CH_3OH via solvent

diffusion. CHN elemental analysis calcd (%) for $C_{160}H_{118}N_{16}Tb_2Cd$: C 65.21, H 4.03, N 15.19; found: C 64.97, H 4.05, N 15.14. ESI−MS; 1476.32 $[M]^{2+}$ (calcd 1476.39)

Mononuclear terbium (III) complex [Tb]

H_2(tertPc) (48 mg, 0.065 mmol), TbPc(CH_3CO_2) (48 mg, 0.066 mmol) were mixed with 3 mL of 1,2,4-trichlorobenzene, 2 mL of 1-hexanol and 0.1 mL of DBU in an N_2 atmosphere. The mixture was refluxed for 2 h in an N_2 atmosphere. The solvent was evaporated in vacuo. Residue was purified by using chromatography over silica gel (Wakogel c-200) with $CHCl_3$ as the eluent. The main green band was collected, and the solvent was evaporated. Further purification of that band by using chromatography on silica gel (Wakogel c-400HG) with $CHCl_3$ as the eluent afforded pure [Tb]. 29 mg (31%) CHN elemental analysis calcd (%) for $C_{80}H_{64}N_{16}Tb$: C 68.22, H 4.58, N 15.91; found: C 68.18, H 4.82, N 15.68. ESI-MS; 1408.48 $[M]^+$ (calcd 1408.47)

Mononuclear yttrium (III) complex [Y]

H_2(tertPc) (150 mg, 0.065 mmol), YPc(CH_3CO_2) (150 mg, 0.066 mmol) were mixed with 9 mL of 1,2,4-trichlorobenzene, 6 mL of 1-hexanol and 0.5 mL of DBU in an N_2 atmosphere. The following procedure is same with that of [Tb]. 155 mg (51%) CHN elemental analysis calcd (%) for $C_{80}H_{64}N_{16}Y$: C 71.79, H 4.82, N 16.74; found: C 71.49, H 4.90, N 16.77.ESI-MS; 1338.47 $[M]^+$ (calcd 1338.46)

Preparation of magnetically diluted sample $[Tb_2]^{2+}$*

$[Tb_2]$ (5.27 mg, 1.56 mmol), [Y] (48.50 mg, 35.90 mmol) were mixed in 10 mL of CH_2Cl_2 by using ultrasonic for 1 h. Phenoxathiin hexachloroantimonate $SbCl_6$·Ox 31.22 mg (58.38 mmol) were mixed in CH_2Cl_2 by using ultrasonication. Addition of an excess amount of hexane afforded a powder sample of diluted $[Tb_2]^{2+}$. Completion of the oxidation reaction was confirmed via UV-Vis-NIR spectrum (Figure S25).

Preparation of magnetically diluted sample $[Tb]^+$*

[Tb] (5.69 mg, 4.04 mmol), [Y] (49.54 mg, 37.01 mmol) were mixed in 10 mL of CH_2Cl_2 by using ultrasonication for 1 h. Phenoxathiin hexachloroantimonate $SbCl_6$·Ox (32.92 mg, 61.56 mmol) were mixed in CH_2Cl_2 by using ultrasonication. Addition of an excess amount of hexane afforded a powder sample of diluted $[Tb]^+$. Completion of the oxidation reaction was confirmed via UV-Vis-NIR spectrum (Figure S25).

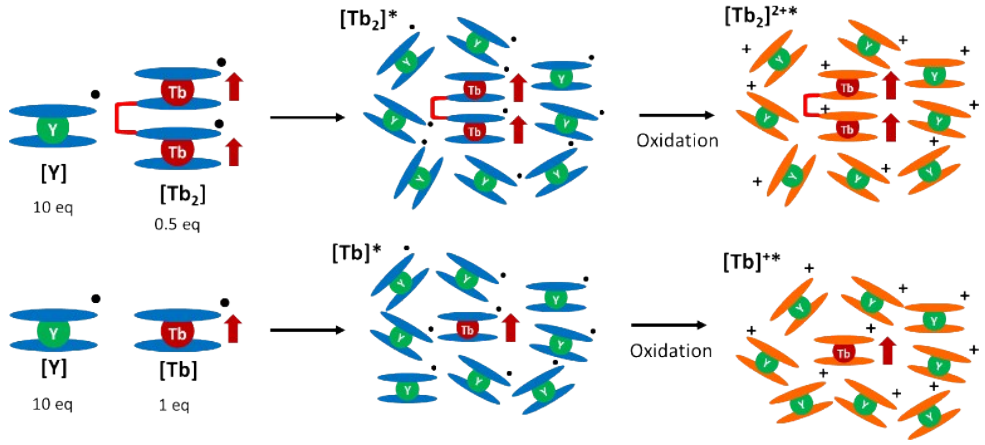

Figure S2. Preparation of magnetically diluted samples. To avoid the intermolecular magnetic interactions and extract the effects of intramolecular Tb−Tb interactions, we prepared magnetically diluted samples ([Tb_2]* and [Tb]*) by doping the Tb(III) complexes into excess amount of [Y]. Because [Tb_2], [Tb] and [Y] have π-radicals on the pthhalocynaninato ligands, and it is known that these π-radical induce the intermolecular magnetic interactions,[4] oxidizer (phenoxathiin hexachloroantimonate:[2] $SbCl_6$·Ox) was added to [Tb_2]* and [Tb]* to quench the radicals as well as the intermolecular magnetic interactions.

Generalized Debye model equations

For fitting ac magnetic susceptibilities, generalized Debye model equations were used.

$$\chi_M' = \chi_S + (\chi_T - \chi_S)\frac{(2\pi\nu\tau)^{1-\alpha}\sin(\frac{\pi\alpha}{2})}{1 + 2(2\pi\nu\tau)^{1-\alpha}\sin(\frac{\pi\alpha}{2}) + (2\pi\nu\tau)^{2-2\alpha}} \qquad \text{eq. S1 (a)}$$

$$\chi_M'' = (\chi_T - \chi_S)\frac{(2\pi\nu\tau)^{1-\alpha}\cos(\frac{\pi\alpha}{2})}{1 + 2(2\pi\nu\tau)^{1-\alpha}\sin(\frac{\pi\alpha}{2}) + (2\pi\nu\tau)^{2-2\alpha}} \qquad \text{eq. S1 (b)}$$

In these equations, χ_S and χ_T are adiabatic and isotherm magnetic susceptibility, respectively, ν is ac frequency of magnetic field, τ is magnetic relaxation time, and α is deviation factor. Both real (χ_M') and imaginary (χ_M'') parts of ac susceptibilities were fitted simultaneously to get τ.

Derivation of equation 1.

Activation energy for spin reversal in a $TbPc_2$ unit is ca. 500 cm^{-1}. Therefore, in the low temperature region, the ground states of the $TbPc_2$ units are $|\pm 6>$. When two $|\pm 6>$ states are coupled together, ferromagnetic $|\pm 6, \pm 6>$ and antiferromagnetic $|\pm 6, \mp 6>$ states are generated. In the case of $[Tb_2]^{2+}$*, it is expected that the $|\pm 6, \pm 6>$ states are more stable than the $|\pm 6, \mp 6>$ states are due to the increase in $\chi_M T$ values in the low temperature regions. If the energy gap between the $|\pm 6, \pm 6>$ and $|\pm 6, \mp 6>$ states is ΔV_{dip}, the axial component of $\chi_M T$ is written as follows according to the Van Vleck equation.

$$\chi_{Mz}T = N_A \frac{\frac{(2g\mu_B J_z)^2}{k_B}}{\exp\left(-\frac{\Delta V_{dip}}{k_B T}\right) + 1} \qquad \text{eq. S2}$$

By subtracting the $\chi_M T$ value at infinite temperature ($N_A(2g\mu_B J_z)/2k_B$), $\Delta\chi_{Mz}T$ was obtained.

$$\Delta\chi_{Mz}T = N_A \frac{\frac{(2g\mu_B J_z)^2}{k_B}}{\exp\left(-\frac{\Delta V_{dip}}{k_B T}\right) + 1} - N_A \frac{(2g\mu_B J_z)^2}{2k_B} \qquad \text{eq. S3}$$

Since equation does not contain the effects of ligand field splitting, we can estimate ΔV_{dip} without considering ligand field splitting. The increase in $\chi_M T$ value at low temperature mainly originates from the axial component of $\Delta\chi_M T$. Therefore, $\Delta\chi_M T \approx \Delta\chi_{Mz}T/3$ is established.

$$\Delta\chi_M T \cong \Delta\chi_{Mz}T/3 = N_A \frac{\frac{(2g\mu_B J_z)^2}{3k_B}}{\exp\left(-\frac{\Delta V_{dip}}{k_B T}\right) + 1} - N_A \frac{(2g\mu_B J_z)^2}{6k_B} \qquad \text{eq. S4}$$

Estimation of the Tb−Tb distance from the magnitude of ΔV_{dip}

Hamiltonian for magnetic dipole-dipole (MD) interactions between dipole_1 and dipole_2 is expressed as eq. S5.

$$V_{dip} = \frac{\mu_0 (g\mu_B)^2}{4\pi R^3}\left\{J^{(1)} \cdot J^{(2)} - 3(J^{(1)} \cdot e)(J^{(2)} \cdot e)\right\} \qquad \text{eq. S5}$$

where μ_0 is magnetic permeability, μ_B is Bohr magnetron, g is Lande g-factor, $\boldsymbol{J}^{(1)}$ and $\boldsymbol{J}^{(2)}$ are angular momentums, R is the distance between $\boldsymbol{J}^{(1)}$ and $\boldsymbol{J}^{(2)}$, and $\boldsymbol{e}$ is the unit vector which connect $\boldsymbol{J}^{(1)}$ and $\boldsymbol{J}^{(2)}$. If the magnetic easy axes of the $TbPc_2$ units are on the same line, eq. S5 becomes simpler due to the absence of perpendicular component of MD interactions:

$$V_{dip} = \frac{\mu_0 (g\mu_B)^2}{4\pi R^3}\left\{\frac{1}{2}(J_+^{(1)} \cdot J_-^{(2)} + J_-^{(1)} \cdot J_+^{(2)}) - 2J_z^{(1)} \cdot J_z^{(2)}\right\} \qquad \text{eq. S6}$$

where $J_{\pm}$ and J_z are lift operators and z component of $\boldsymbol{J}$. When considering the $|\pm 6, \pm 6>$ and $|\pm 6, \mp 6>$ states as the ground states, matrix elements can be derived from eq. S5 as follows:

	$\|\pm 6, \pm 6>$	$\|\pm 6, \mp 6>$
$<\pm 6, \pm 6\|$	$\frac{-18\mu_0(g\mu_B)^2}{\pi R^3}$	
$<\pm 6, \mp 6\|$		$\frac{18\mu_0(g\mu_B)^2}{\pi R^3}$

Therefore, the energy gap between the $|\pm 6, \pm 6>$ and $|\pm 6, \mp 6>$ states (ΔV_{dip}) is as follows:

$$\Delta V_{dip} = \frac{36\mu_0(g\mu_B)^2}{\pi R^3} \qquad \text{eq. S7}$$

By using eq. S7 and ΔV_{dip} = 0.646 cm^{-1}, R was estimated to be 6.01 Å.

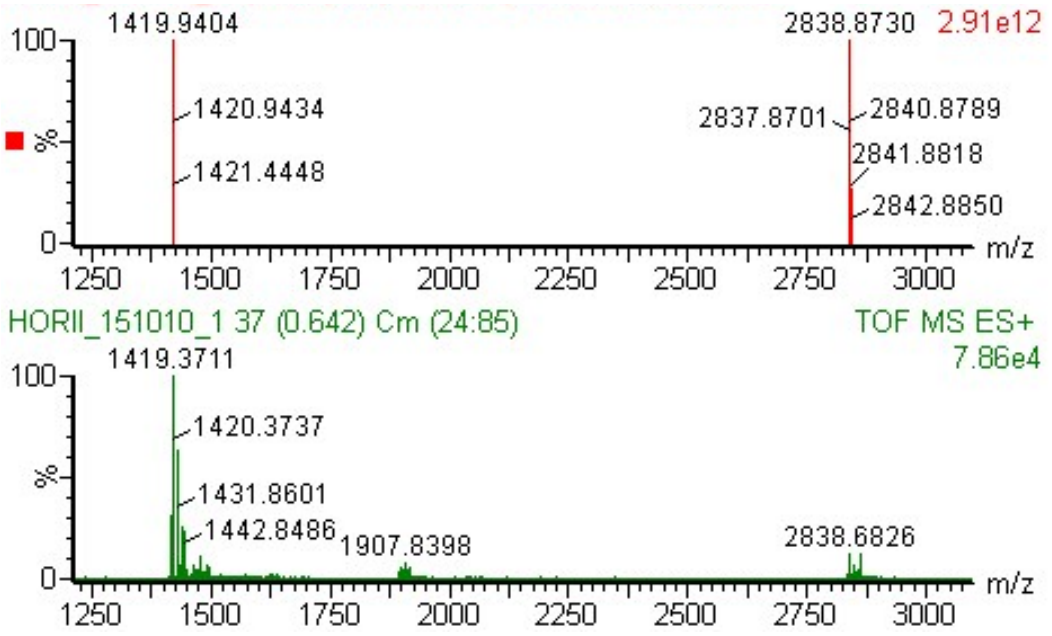

Figure S3. Experimental (below) and calculated (above) ESI mass spectra for [Tb_2].

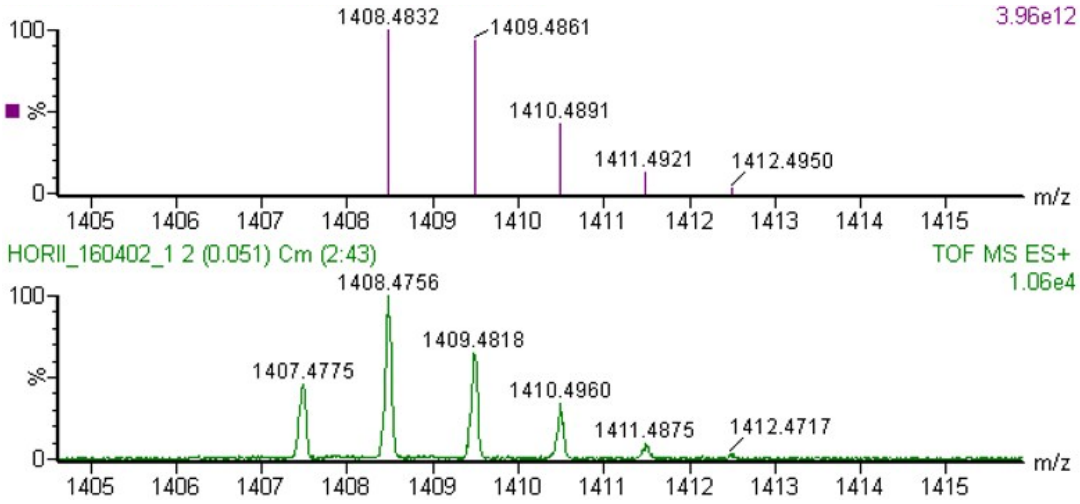

Figure S4. Experimental (below) and calculated (above) ESI mass spectra for [Tb].

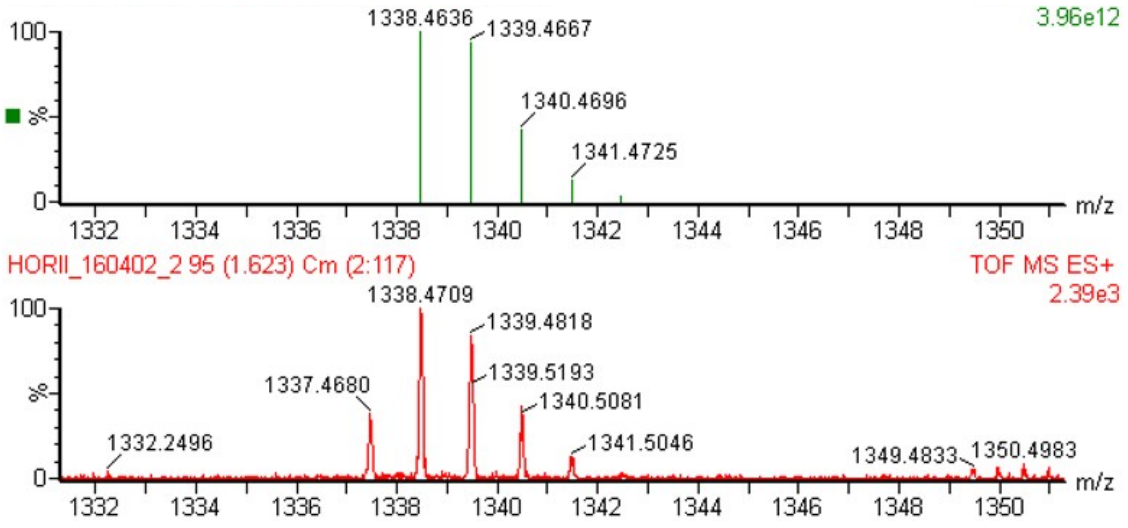

Figure S5. Experimental (below) and calculated (above) isotope pattern for [Y] shown in ESI mass spectrum.

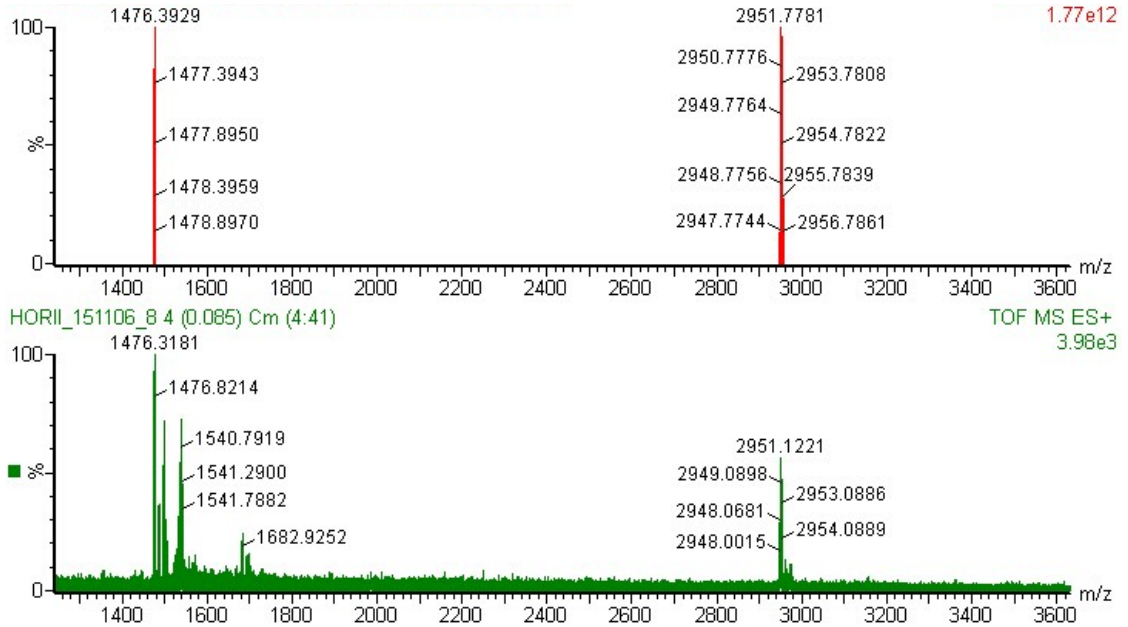

Figure S6. Experimental (below) and calculated (above) ESI mass spectra for [Tb_2Cd].

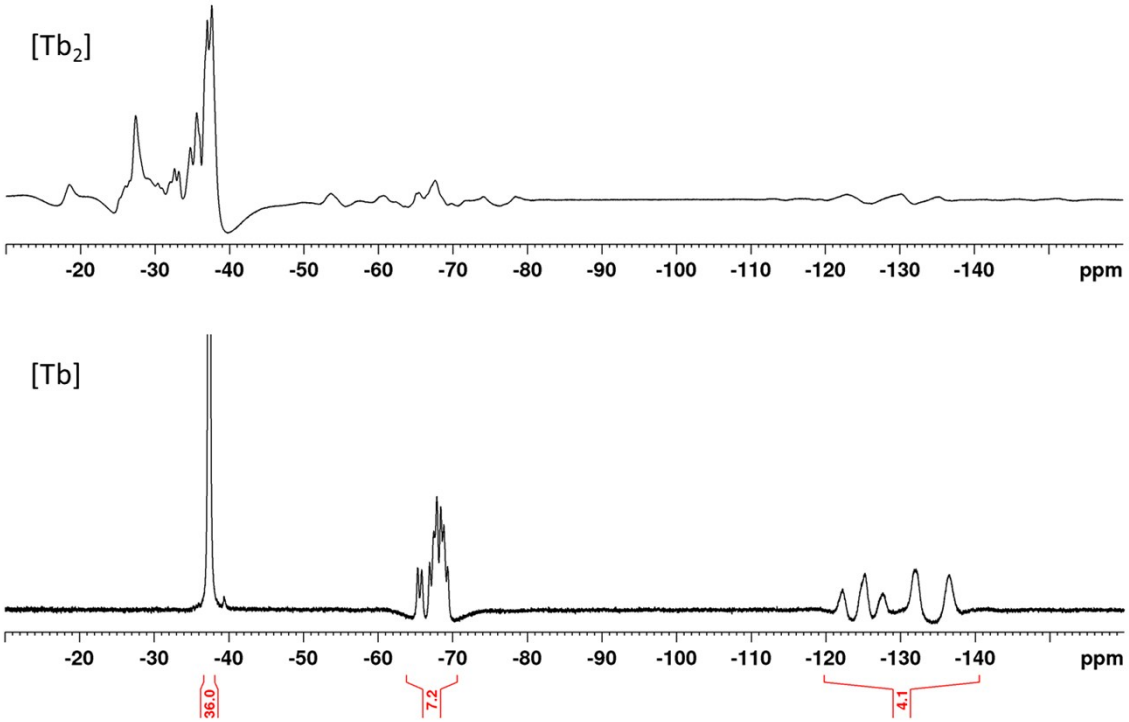

Figure S7. ^{1}H NMR spectra for [Tb_2] and [Tb] dissolved in CD_2Cl_2. Paramagnetic behaviors and low molecular symmetries of [Tb_2] and [Tb] make it difficult to obtain sharp NMR spectra. It is especially difficult to assign the spectra for [Tb_2]. In contrast, the ^{1}H NMR spectra for [Tb] are relatively sharper. The signal at –37.36 ppm originates from tertiary butyl group in [Tb].

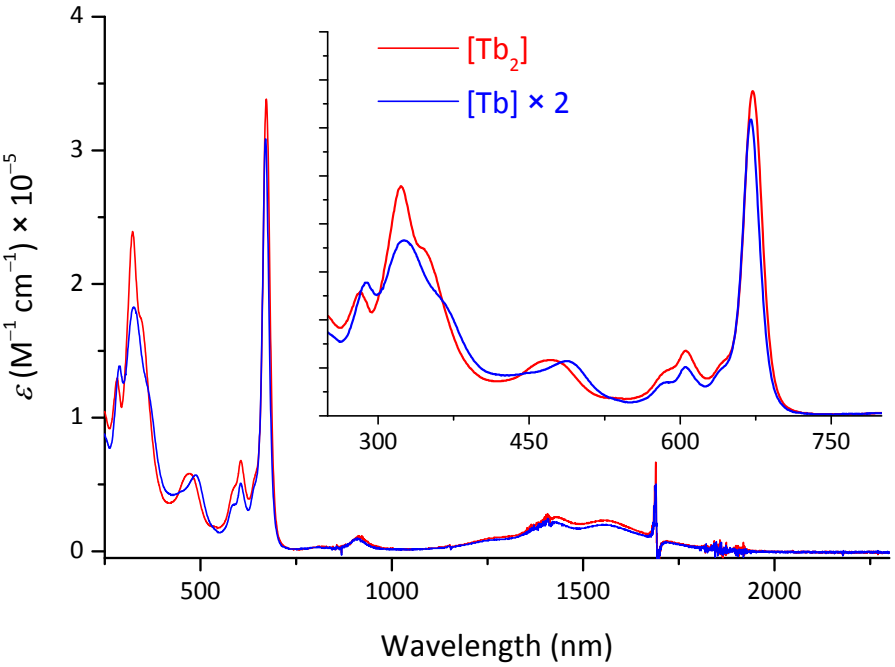

Figure S8. UV-Vis-NIR spectrum of [Tb_2] and [Tb].

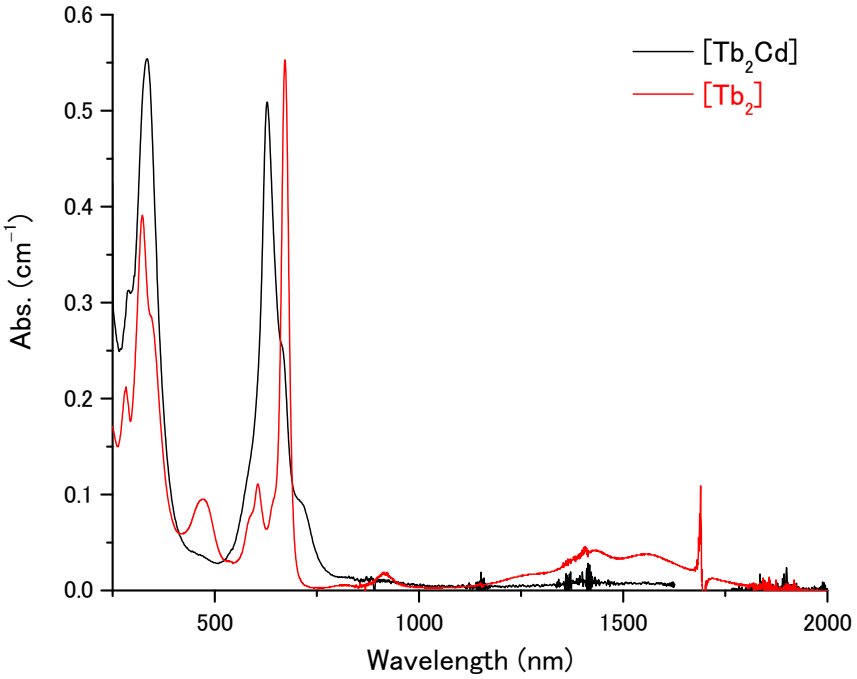

Figure S9. UV-Vis-NIR spectrum of [Tb_2] and [Tb_2Cd]. Absence of the broad NIR band indicates the absence of a π-radical in [Tb_2Cd].

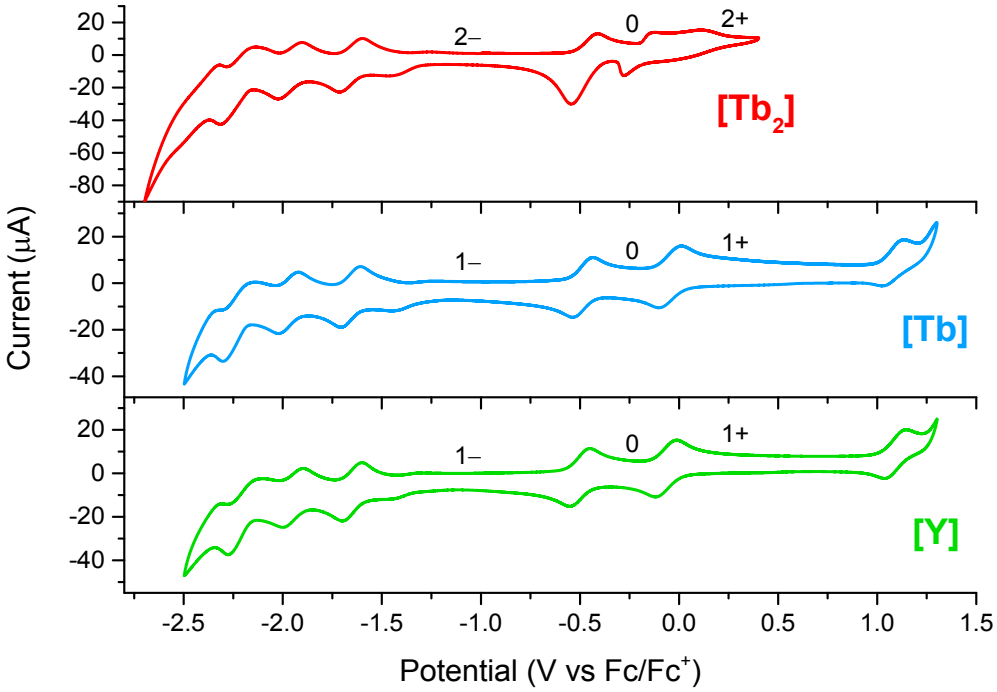

Figure S10. Cyclic voltammogram (CV) of [Tb_2], [Tb] and [Y].

Table S1. Redox potentials obtained from the DPV measurements (V vs Fc/Fc^+). Ox2 corresponds to the potentials for $LnPc_2/LnPc_2^+$

	Red3	Red2	Red1	Ox1	Ox2	Ox3
[Tb_2]	–2.225	–1.960	–1.654	–0.206	**–0.477**	
[Tb]	–2.226	–1.970	–1.658	–0.484	**–0.047**	1.081
[Y]	–2.197	–1.940	–1.647	–0.499	**–0.061**	1.094

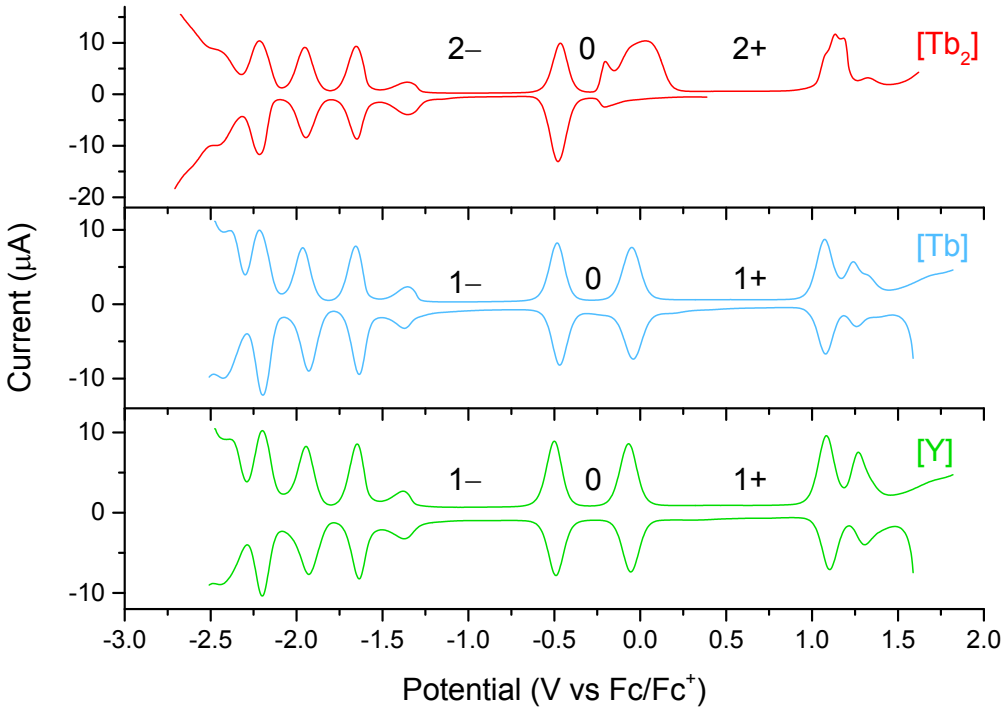

Figure S11. Differential plus voltammetry (DPV) of [Tb_2], [Tb] and [Y].

Table S2. Redox potentials obtained from the DPV measurements (V vs Fc/Fc^+). Ox2 correspond to the potentials for $LnPc_2/LnPc_2^+$

	Red3	Red2	Red1	Ox1	**Ox2**	Ox3	Ox4
[Tb_2]	–2.212	–1.948	–1.652	–0.464	**–0.204**	1.136	1.180
[Tb]	–2.216	–1.964	–1.656	–0.484	**–0.048**	1.072	1.240
[Y]	–2.200	–1.944	–1.648	–0.500	**–0.068**	1.084	1.268

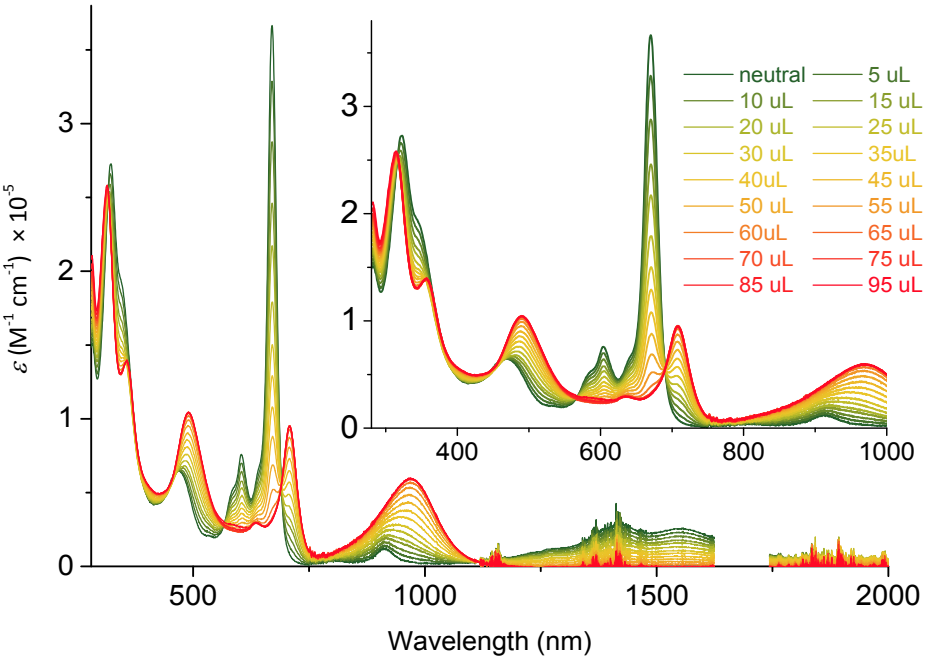

Figure S12. Changes in the UV-Vis-NIR spectrum upon the addition of $SbCl_6$·Ox solution (0.319 mM) to [Tb_2] in CH_2Cl_2. Observation of isosbestic points indicate no decomposition of [Tb_2] during the oxidation reactions.

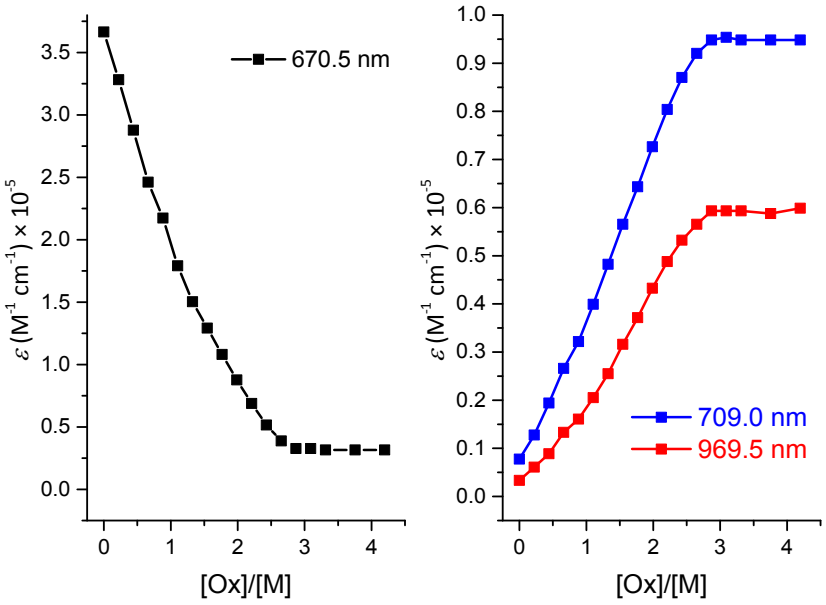

Figure S13. Changes in molar absorption coefficient ε (M^{-1} cm^{-1}) of [Tb] during oxidative titration. ε became constant above 2.5 [Ox]/[M], meaning that 2.5 equivalent of $SbCl_6$·Ox is required for complete conversion of [Tb_2] into $[Tb_2]^{2+}$.

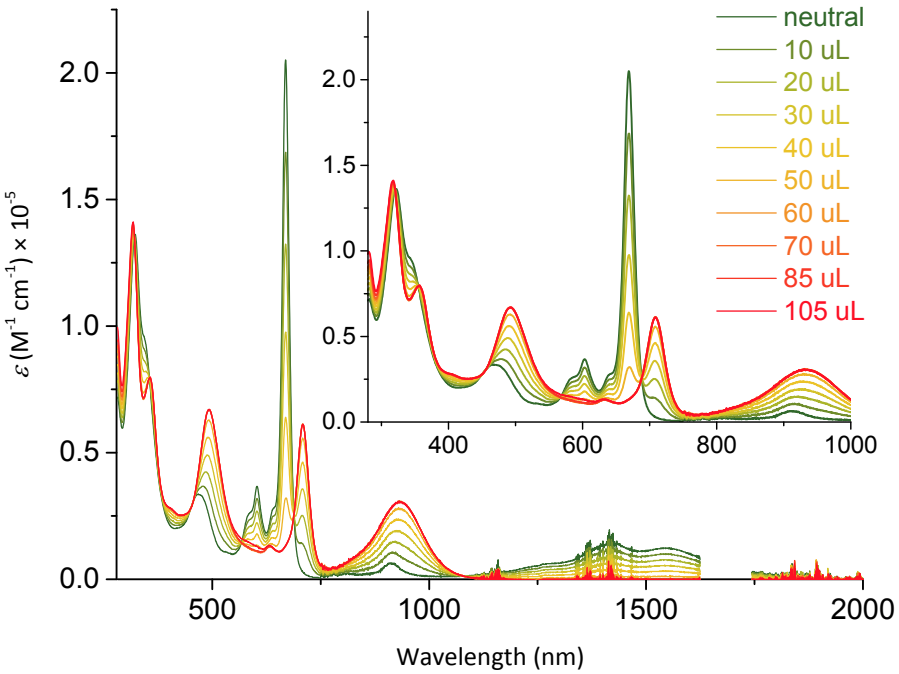

Figure S14. Changes in UV-Vis-NIR spectrum upon addition of $SbCl_6$·Ox solution (0.319 mM) to [Tb] in CH_2Cl_2. Observation of the isosbestic points indicate no decomposition of [Tb] during the oxidation reactions.

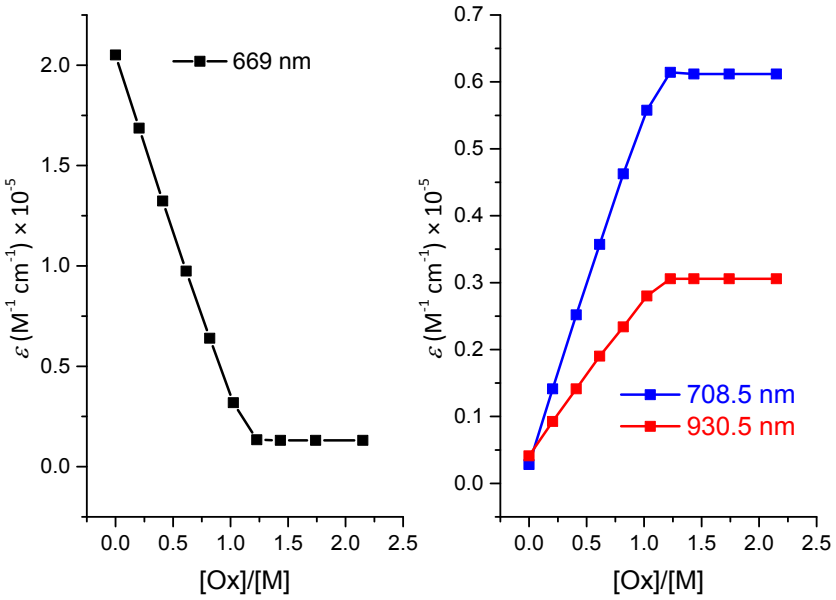

Figure S15. Changes in molar absorption coefficient ε (M^{-1} cm^{-1}) of [Tb] during oxidative titration. ε became constant above 1.25 [Ox]/[M], meaning that 1.25 equivalent of $SbCl_6$·Ox is required for complete conversion of [Tb] into $[Tb]^+$.

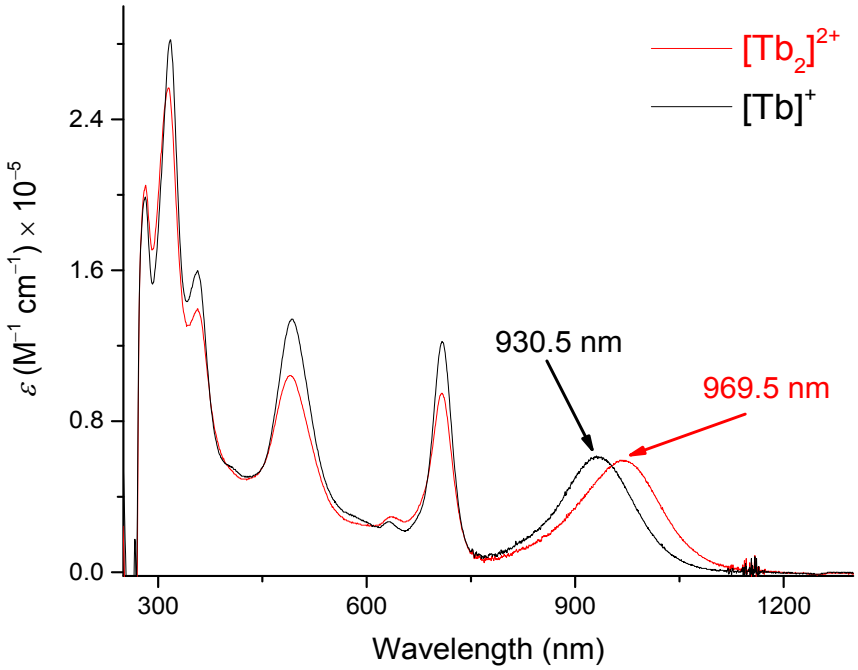

Figure S16. UV-Vis-NIR spectrum of $[Tb_2]^{2+}$ and $[Tb]^{+}$ in CH_2Cl_2

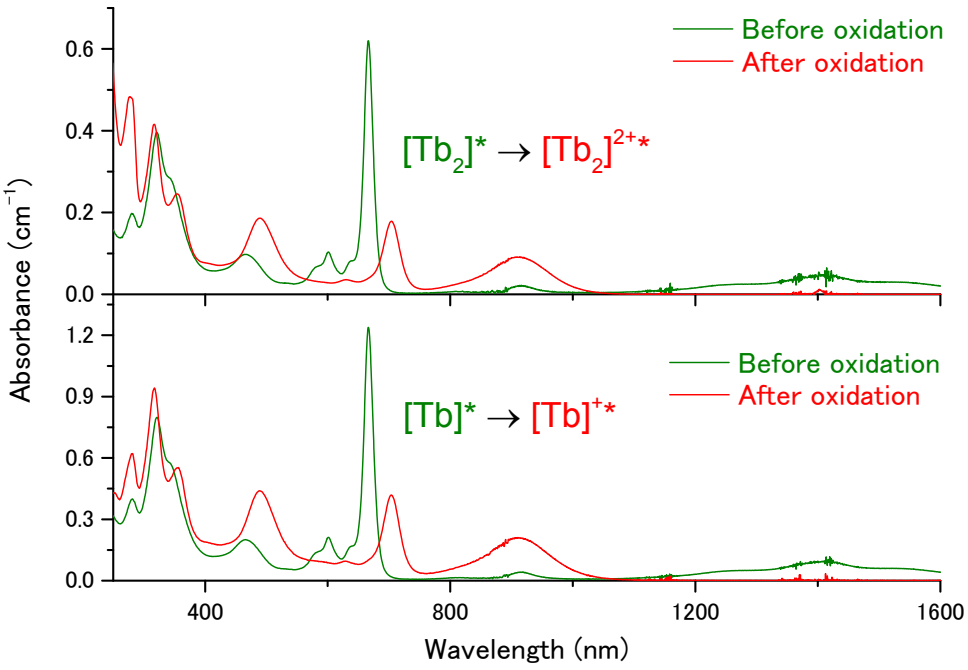

Figure S17. Changes in UV-Vis-NIR spectrum before and after oxidation of $[Tb_2]^*$ and $[Tb]^*$ in CH_2Cl_2.

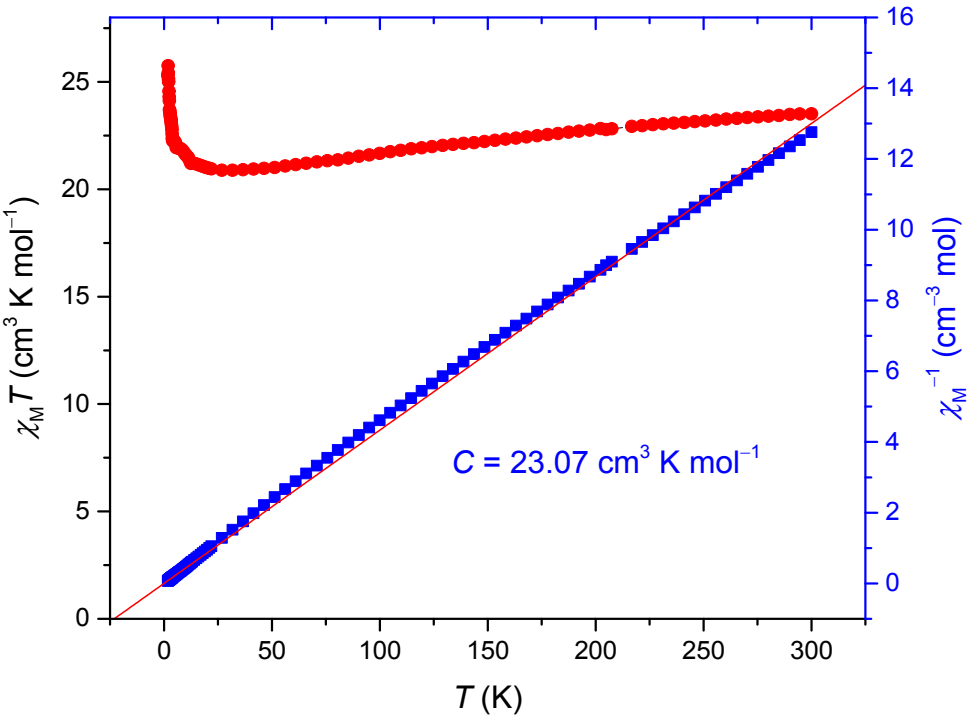

Figure S18. $\chi_M T$ vs T and χ_M^{-1} vs T plots for [Tb_2] in a 1000 Oe dc magnetic field. Solid line on the χ_M^{-1} vs T plots was fitted using the Curie equation for $T > 150$ K

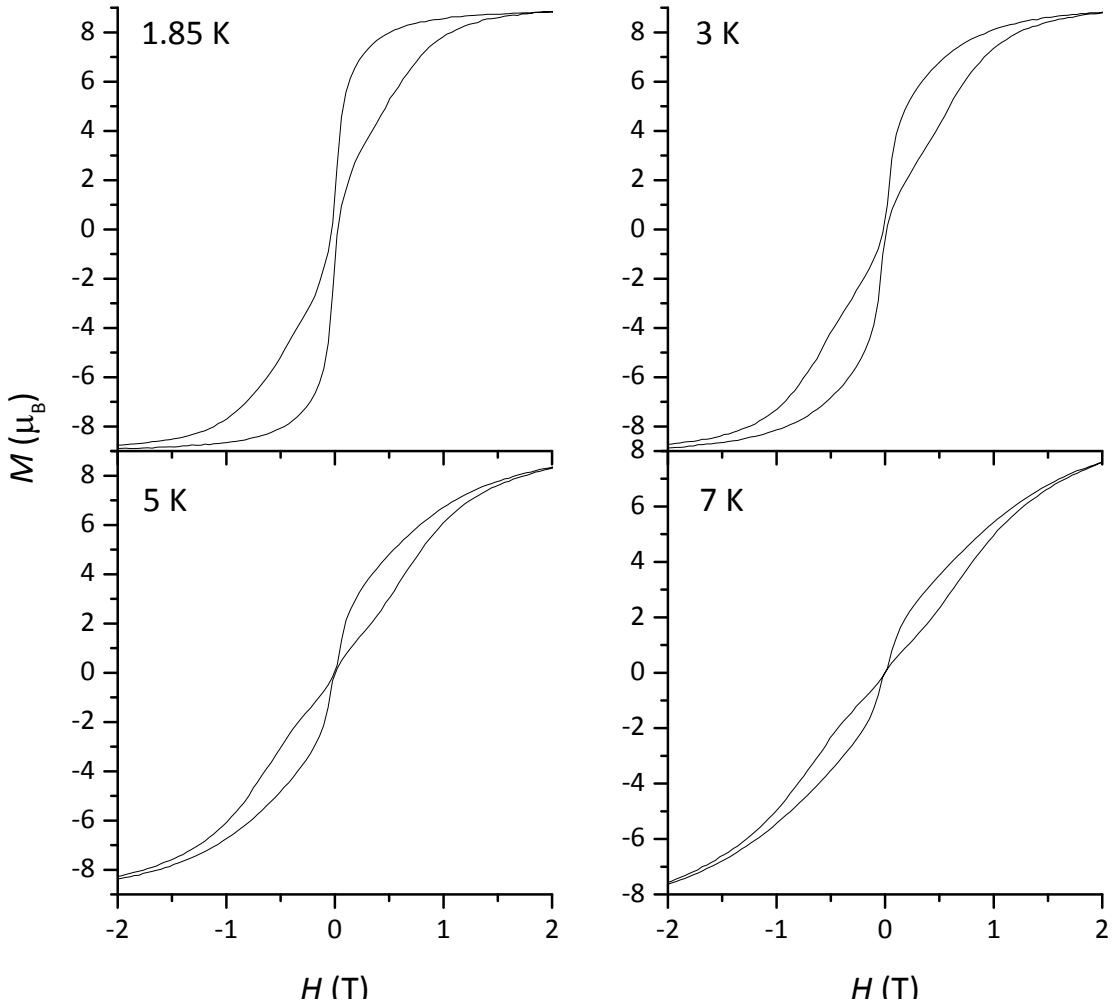

Figure S19. *MH* curves for [Tb_2] at a field sweep rate of 15 Oe/s.

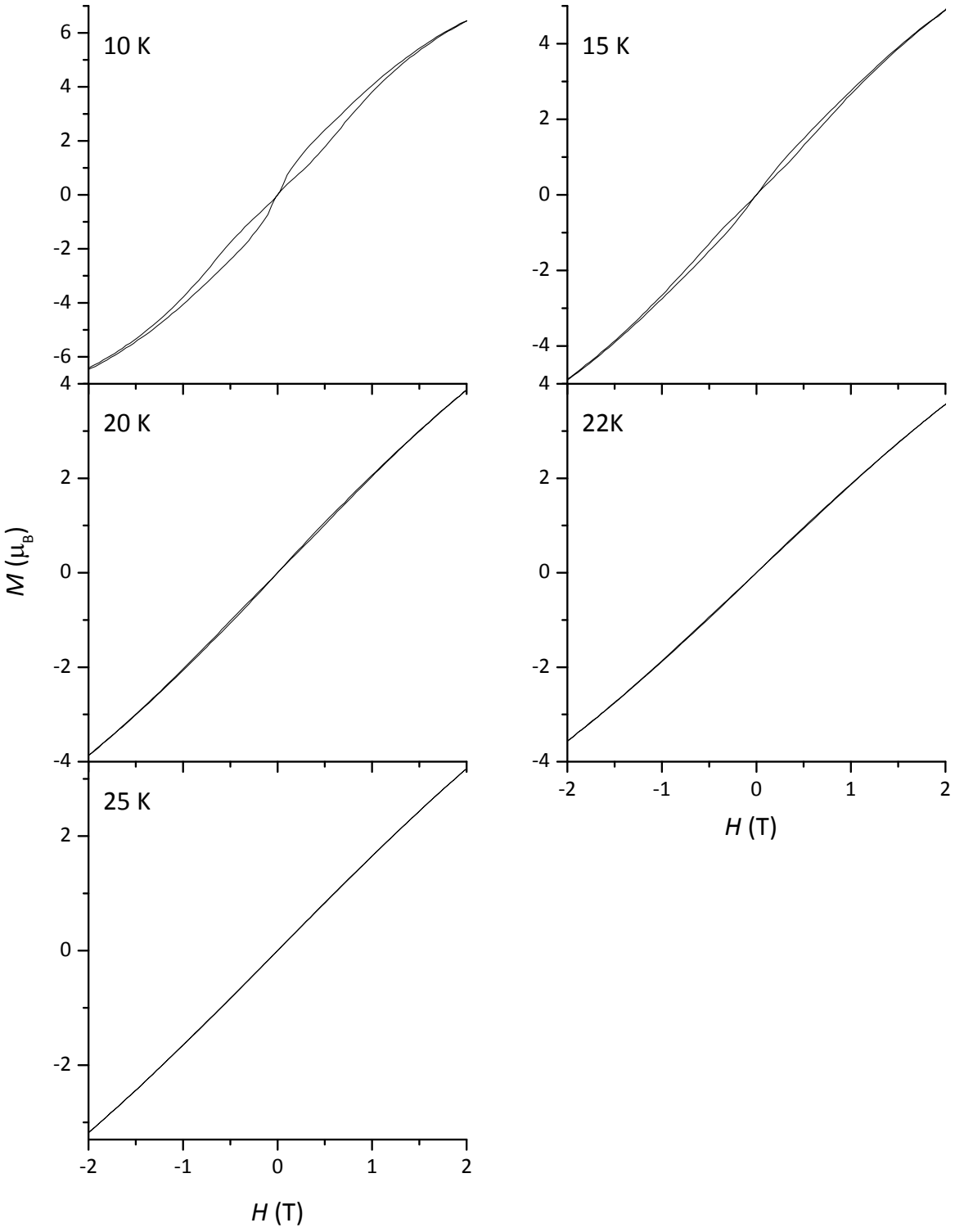

Figure S20. *MH* curves for [Tb_2] at a field sweep rate of 15 Oe/s.

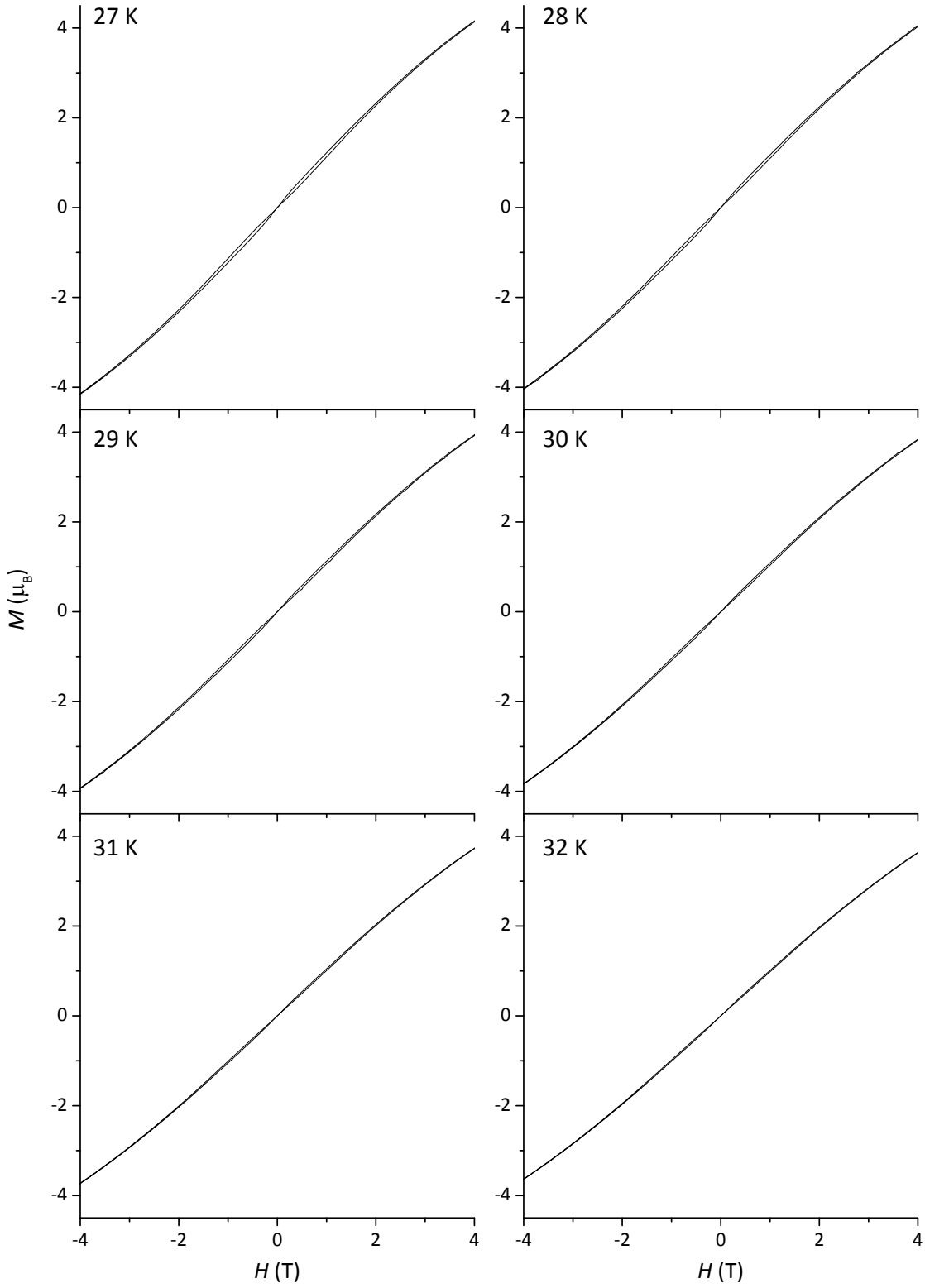

Figure S21. *MH* curves for [Tb_2] at a field sweep rate of 200 Oe/s.

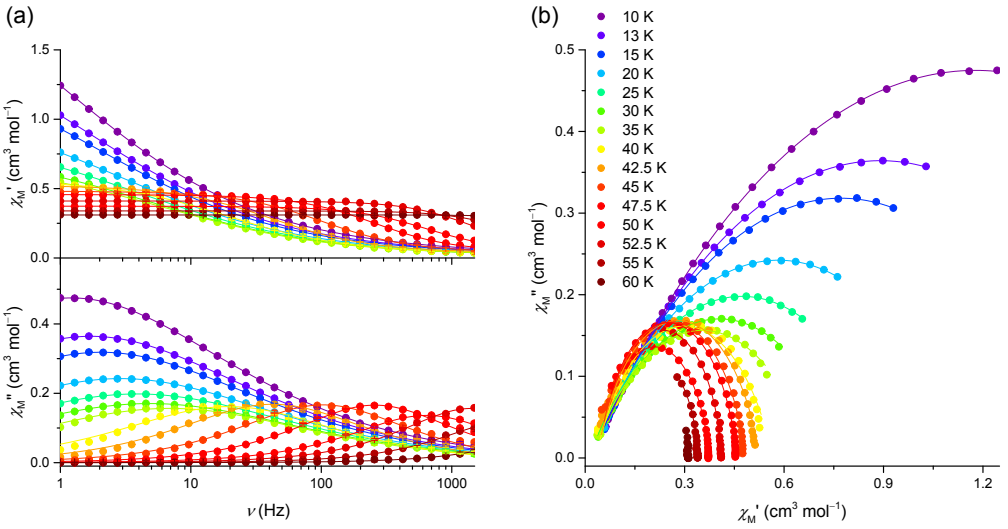

Figure S22. (a) χ_M' vs ν and χ_M'' vs ν plots (b) Cole-Cole plots for [Tb_2] without an applied dc magnetic field. Solid lines were fitted using the Debye model.

Table S3. Fitting parameter obtained from Figure S22.

T (K)	χ_s (cm^3 mol^{-1})	dev(χ_s)	χ_T (cm^3 mol^{-1})	dev(χ_T)	τ (s)	dev(τ)	α	dev(α)
10	0.02019	6.91593E−4	2.33528	0.0066	0.13105	0.00126	0.50433	9.33467E−4
13	0.01853	6.98687E−4	1.76282	0.00523	0.09327	9.32524E−4	0.49629	0.00113
15	0.01813	6.46928E−4	1.52469	0.00426	0.0776	7.23471E−4	0.49106	0.00115
20	0.01213	7.30915E−4	1.15344	0.00377	0.05496	5.94595E−4	0.48877	0.00152
25	0.00982	8.02018E−4	0.93583	0.00338	0.04101	4.86197E−4	0.48548	0.00188
30	0.01021	9.10486E−4	0.79926	0.0033	0.03277	4.40508E−4	0.481	0.00234
35	0.01623	0.00169	0.69043	0.00488	0.02313	5.08648E−4	0.44705	0.00483
40	0.03191	0.00292	0.56649	0.00426	0.00814	1.91181E−4	0.30743	0.00915
42.5	0.03588	0.00275	0.52707	0.00262	0.00374	6.71167E−5	0.23513	0.00815
45	0.03872	0.00259	0.48341	0.00158	0.00154	2.21418E−5	0.18155	0.00701
47.5	0.04271	0.00226	0.45743	8.39632E−4	6.16728E−4	6.54056E−6	0.14148	0.00516
50	0.04719	0.00269	0.37366	5.11067E−4	2.47702E−4	3.32544E−6	0.11524	0.00552
52.5	0.06116	0.00441	0.41058	3.64938E−4	1.1256E−4	2.06112E−6	0.07098	0.00556
55	0.08339	0.00819	0.33929	2.53869E−4	5.84189E−5	2.55548E−6	0.04643	0.00858
60	0	0.17342	0.31033	2.26556E−4	1.0729E−5	7.01628E−6	0.02784	0.03063

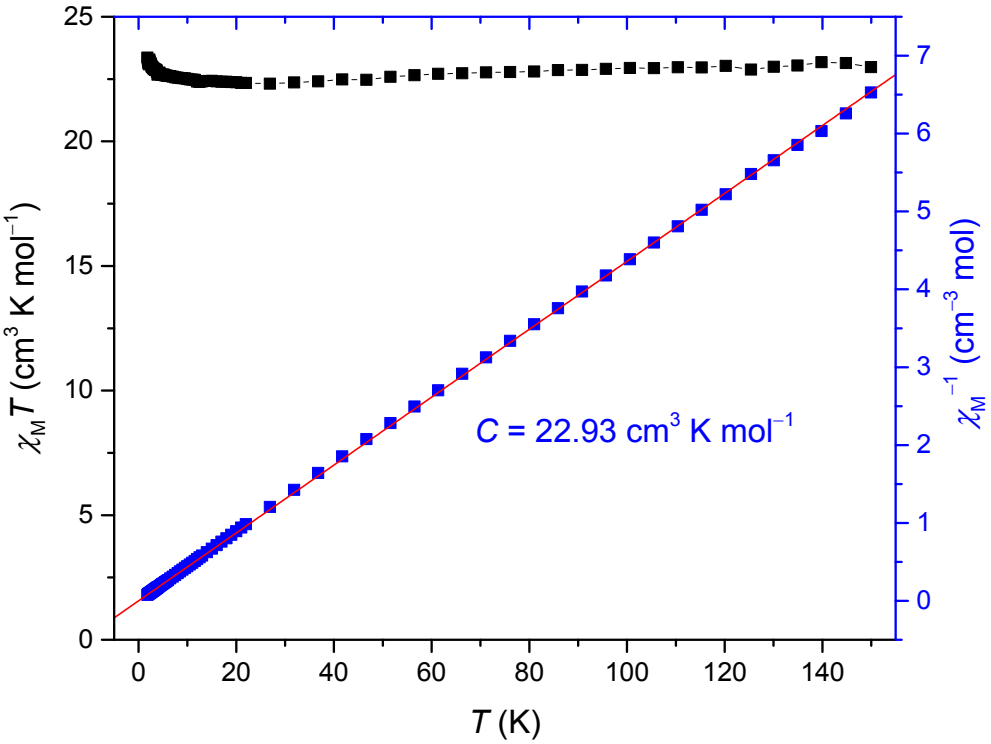

Figure S23. $\chi_M T$ vs T and χ_M^{-1} vs T plots for [Tb_2] in the frozen solution of CH_2Cl_2 at 1000 Oe dc magnetic field. Measurements were performed below a melting point of CH_2Cl_2 (175.7 K) Solid line in the χ_M^{-1} vs T plots were fitted using the Curie equation for $T > 100$ K.

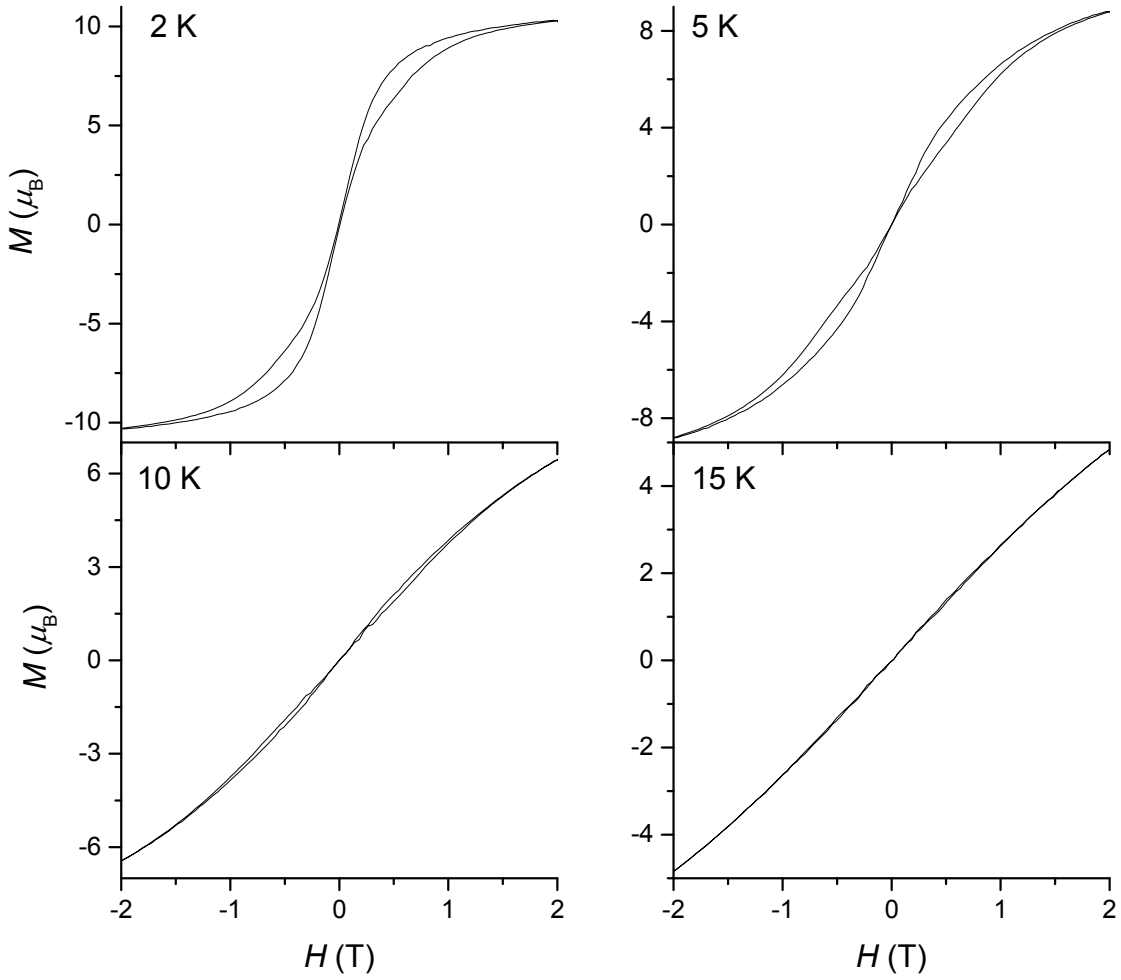

Figure S24. *MH* curves for [Tb_2] at a field sweep rate of 15 Oe/s.

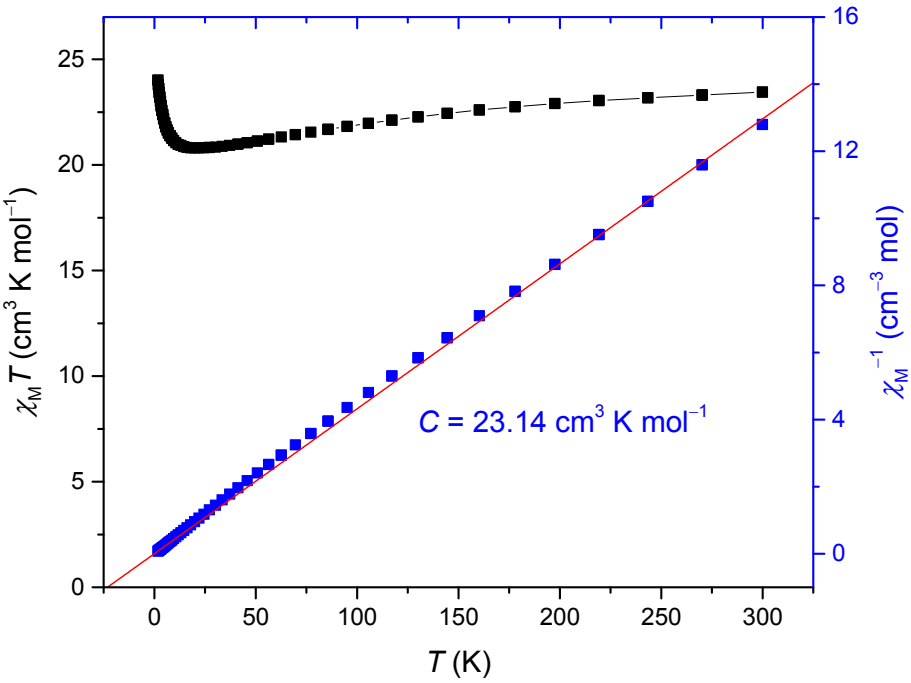

Figure S25. $\chi_M T$ vs T and χ_M^{-1} vs T plots for [Tb_2Cd] in a 1000 Oe dc magnetic field. Solid line in the χ_M^{-1} vs T plots were fitted using the Curie equation for T > 150 K.

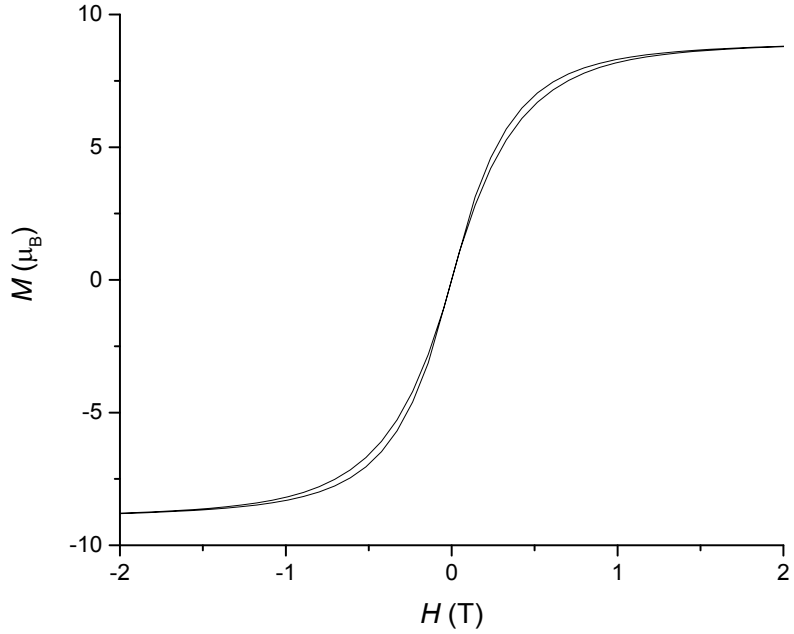

Figure S26. *MH* curves for [Tb_2Cd] at 2 K and a field sweep rate of 15 Oe/s.

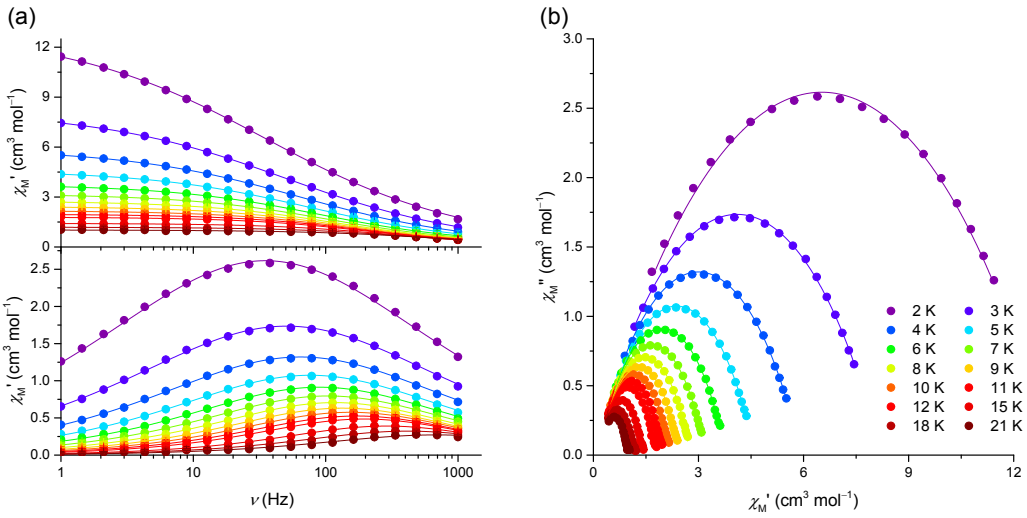

Figure S27. (a) χ_M' vs ν and χ_M'' vs ν plots (b) Cole−Cole plots for [Tb_2Cd] without an applied dc magnetic field. Solid lines were fitted using the Debye model.

Table S4. Fitting parameter obtained from Figure S27.

T (K)	χ_s (cm^3 mol^{-1})	dev(χ_s)	χ_T (cm^3 mol^{-1})	dev(χ_T)	τ (s)	dev(τ)	α	dev(α)
2	0	0.05021	13.04052	0.04724	0.00454	6.40361E−5	0.51428	0.0037
3	0	0.02197	8.21106	0.01645	0.00314	2.8152E−5	0.49091	0.00241
4	0.07001	0.0179	5.92308	0.01152	0.00246	2.39922E−5	0.46049	0.0027
5	0.13532	0.01223	4.61359	0.0071	0.00208	1.73672E−5	0.43046	0.0024
6	0.1384	0.01402	3.77231	0.00735	0.00177	2.00092E−5	0.40686	0.00335
7	0.14458	0.01102	3.19303	0.00531	0.00154	1.57497E−5	0.38739	0.00309
8	0.16004	0.01306	2.7632	0.00585	0.00136	1.8733E−5	0.36696	0.00426
9	0.16705	0.01286	2.43967	0.0053	0.00119	1.79543E−5	0.35402	0.00468
10	0.14961	0.01424	2.18284	0.00537	0.00104	1.8853E−5	0.34367	0.0056
11	0.15962	0.01618	1.97271	0.00569	9.25571E−4	2.08657E−5	0.33062	0.00699
12	0.15033	0.02024	1.79454	0.00652	8.11613E−4	2.46299E−5	0.32102	0.00932
15	0.12545	0.02854	1.42054	0.0071	5.51366E−4	2.85613E−5	0.30874	0.01478
18	0.10059	0.03167	1.19084	0.00576	3.81884E−4	2.62947E−5	0.31994	0.0164
21	0.04126	0.06326	1.0226	0.00744	2.31028E−4	3.72848E−5	0.35591	0.02795

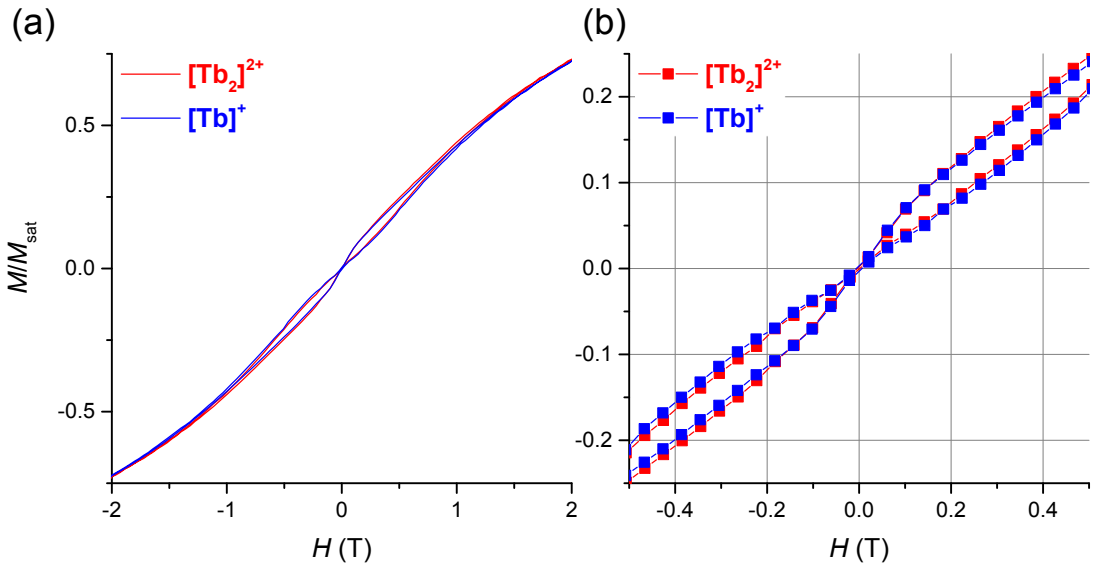

Figure S28. (a) Comparison of *MH* curves for $[Tb_2]^{2+}$* and $[Tb]^{+}$* at 10 K. (b) Enlarged view. There are no obvious differences between the plots.

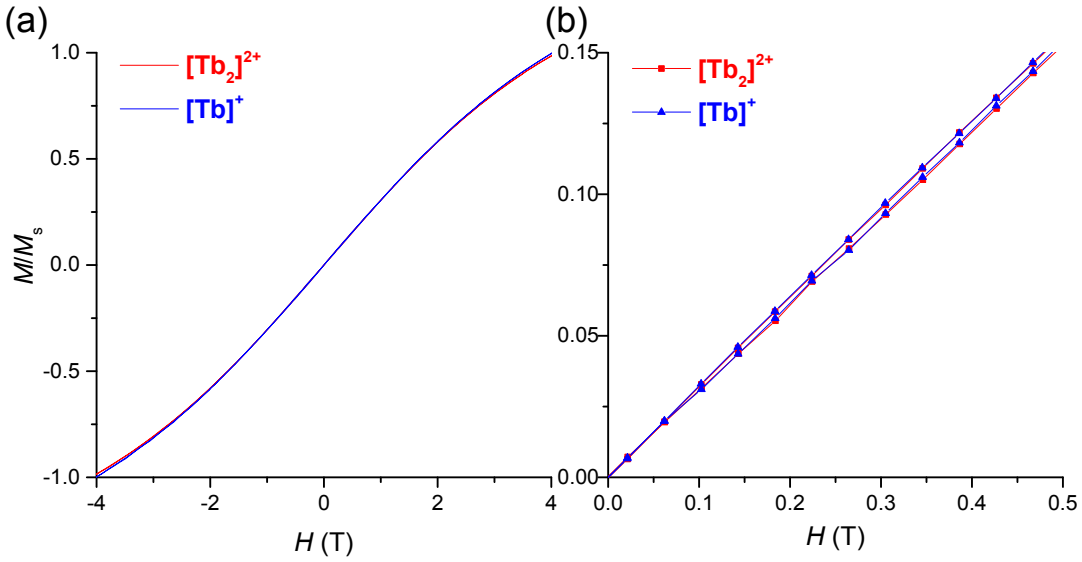

Figure S29. (a) Comparison of *MH* curves for $[Tb_2]^{2+}$* and $[Tb]^{+}$* at 20 K. (b) Enlarged view. There are no obvious differences between the two plots.

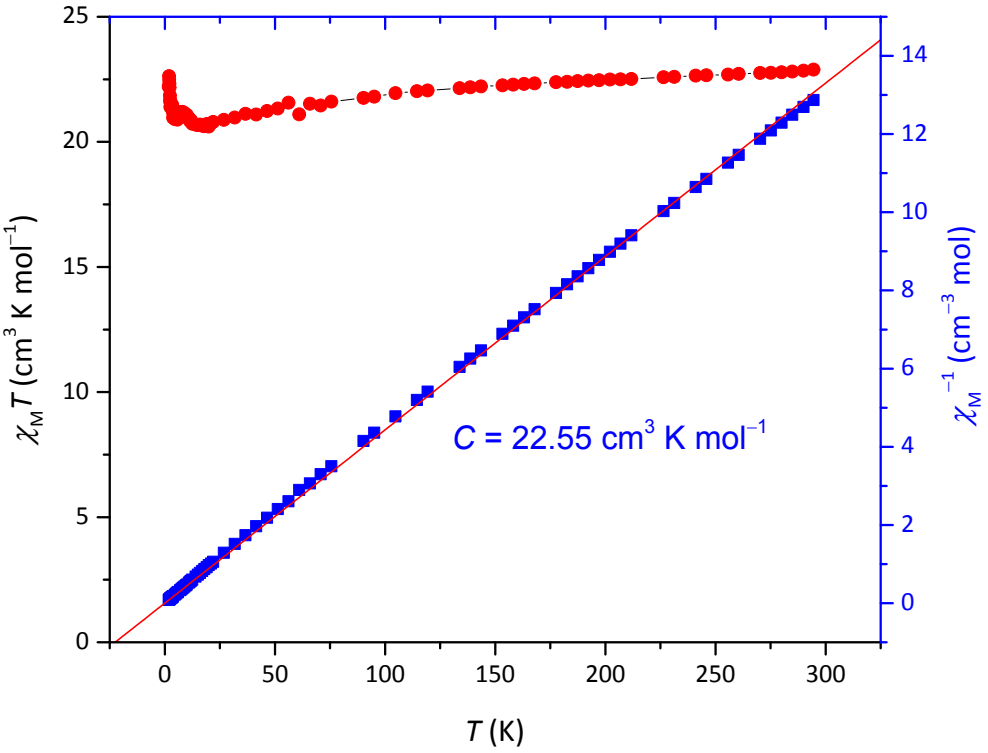

Figure S30. $\chi_M T$ vs T and χ_M^{-1} vs T plots for $[Tb_2]^{2+}$* in a 1000 Oe dc magnetic field. Solid lines in the χ_M^{-1} vs T plots were fitted using the Curie equation for $T > 200$ K. The Curie constant is smaller than the expected value (C = 23.262 cm^3 K mol^{-1} for 2 mole of Tb(III)) due to the magnetic dilution.

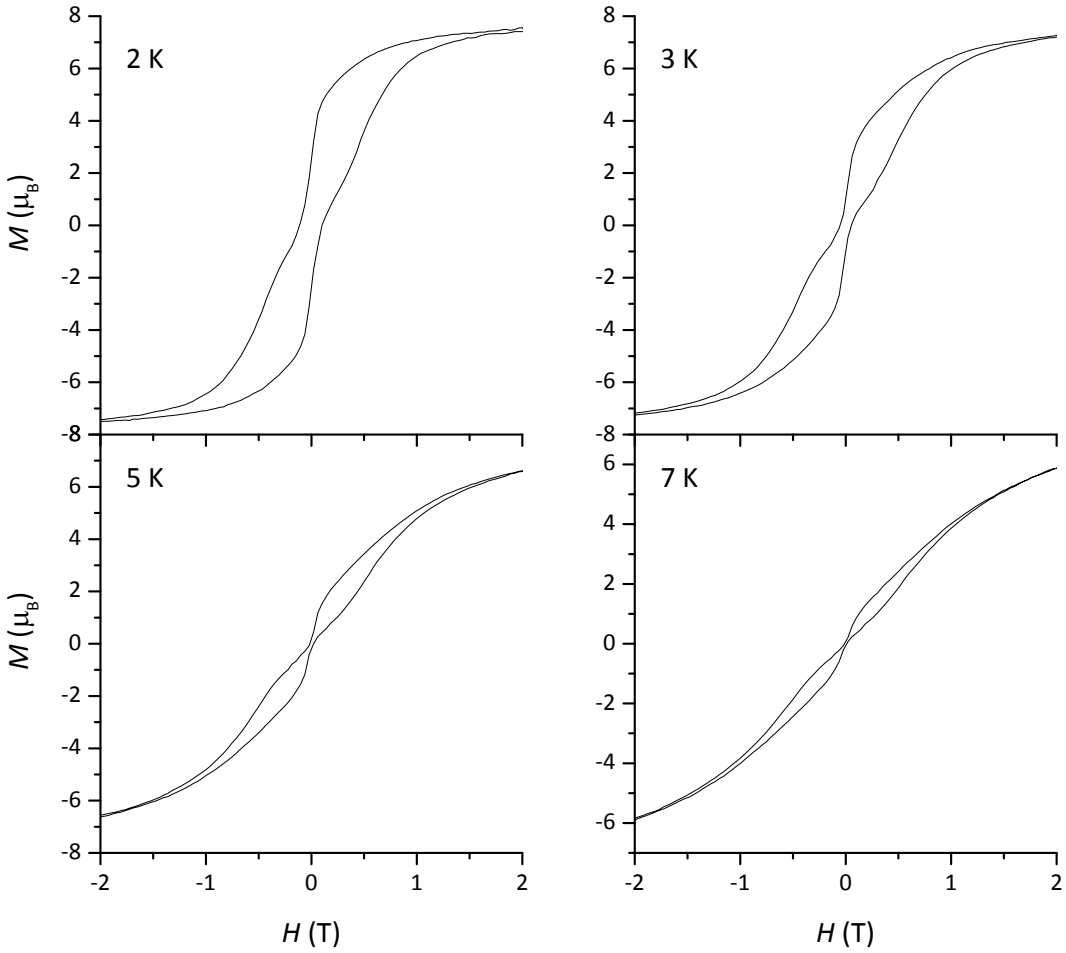

Figure S31 *MH* curves for $[Tb_2]^{2+}$* at 2 K and a field sweep rate of 15 Oe/s.

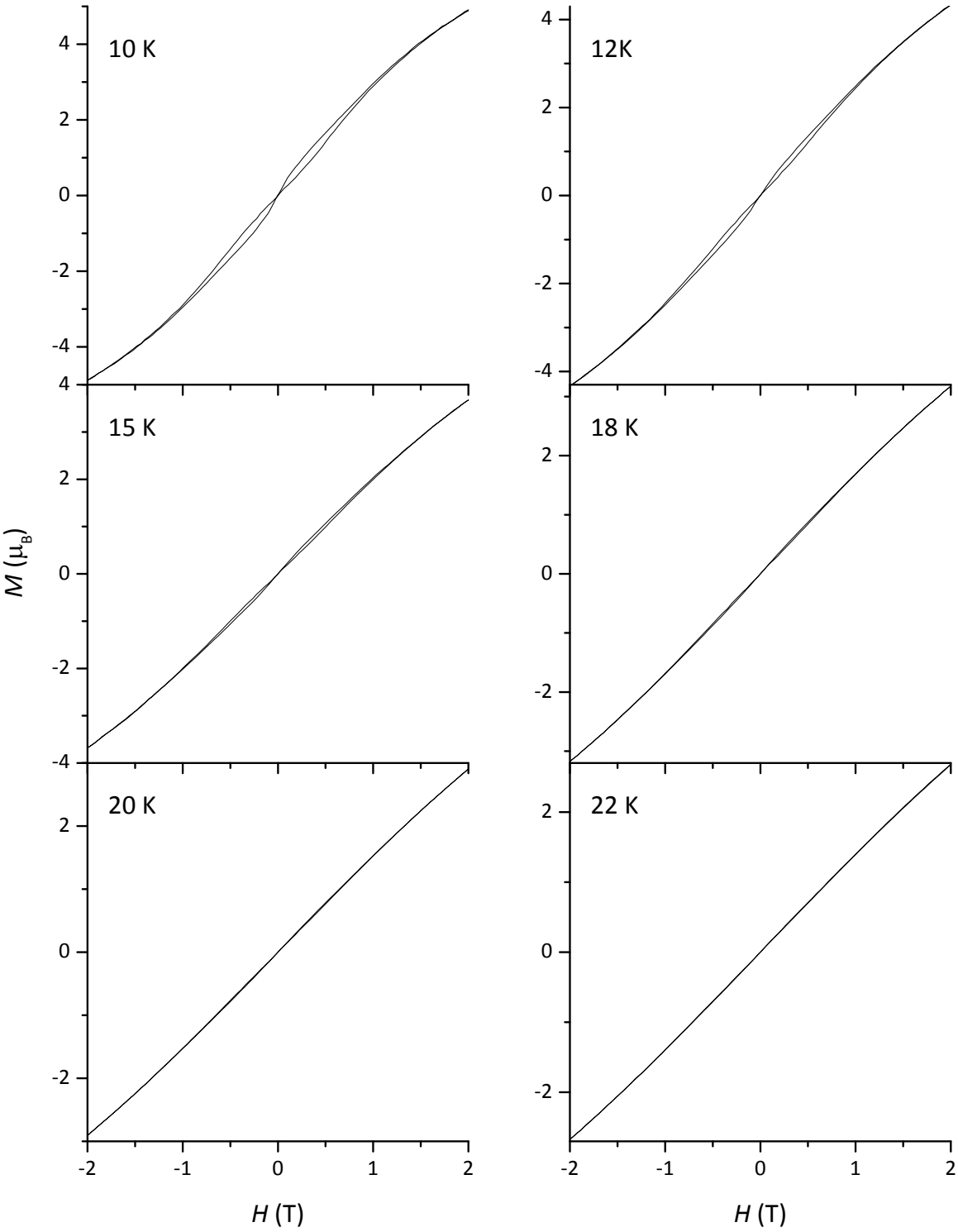

Figure S32. *MH* curves for $[Tb_2]^{2+}$* at 2 K and a field sweep rate of 15 Oe/s.

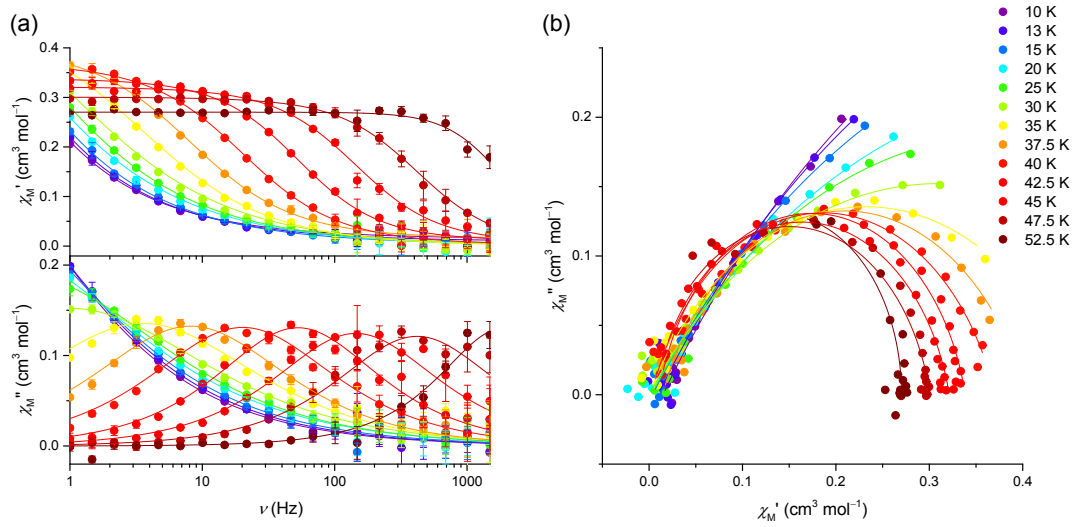

Figure S33. (a) χ_M' vs ν and χ_M'' vs ν plots (b) Cole−Cole plots for $[Tb_2]^{2+}$* without an applied dc magnetic field. Solid lines were fitted using the Debye model.

Table S5. Fitting parameter obtained from Figure S33.

T (K)	χ_S (cm^3 mol^{-1})	dev(χ_S)	χ_T (cm^3 mol^{-1})	dev(χ_T)	τ (s)	dev(τ)	α	dev(α)
10	0.0012	1.45717	0.13374	1.93183	0.39556	0.39845	0.00833	0.0012
13	9.17289E−4	1.10031	0.08819	0.99292	0.18559	0.38309	0.00974	9.17289E−4
15	9.583E−4	1.11591	0.1054	1.02503	0.2407	0.40691	0.01115	9.583E−4
20	0.00236	0.90043	0.06741	0.59982	0.11646	0.42617	0.01351	0.00236
25	0.00208	0.92199	0.10643	0.56892	0.17081	0.43945	0.0158	0.00208
30	0.00243	0.59656	0.01433	0.14924	0.0096	0.40167	0.01078	0.00243
35	0.00351	0.43937	0.00405	0.03981	9.42218E−4	0.295	0.01358	0.00351
37.5	0.00277	0.40193	0.00462	0.02201	3.4703E−4	0.19776	0.01303	0.00277
40	0.00468	0.35794	0.00178	0.00889	2.39482E−4	0.13818	0.01055	0.00468
42.5	0.004	0.34057	0.00166	0.00321	6.94596E−5	0.12252	0.00959	0.004
45	0.00657	0.31595	0.00125	9.69328E−4	3.93095E−5	0.12435	0.01421	0.00657
47.5	0.00434	0.30029	4.49195E−4	4.62052E−4	1.45272E−5	0.08991	0.01551	0.00434
52.5	0.04613	0.26931	7.60788E−4	8.95634E−5	2.33285E−5	0	0.03641	0.04613

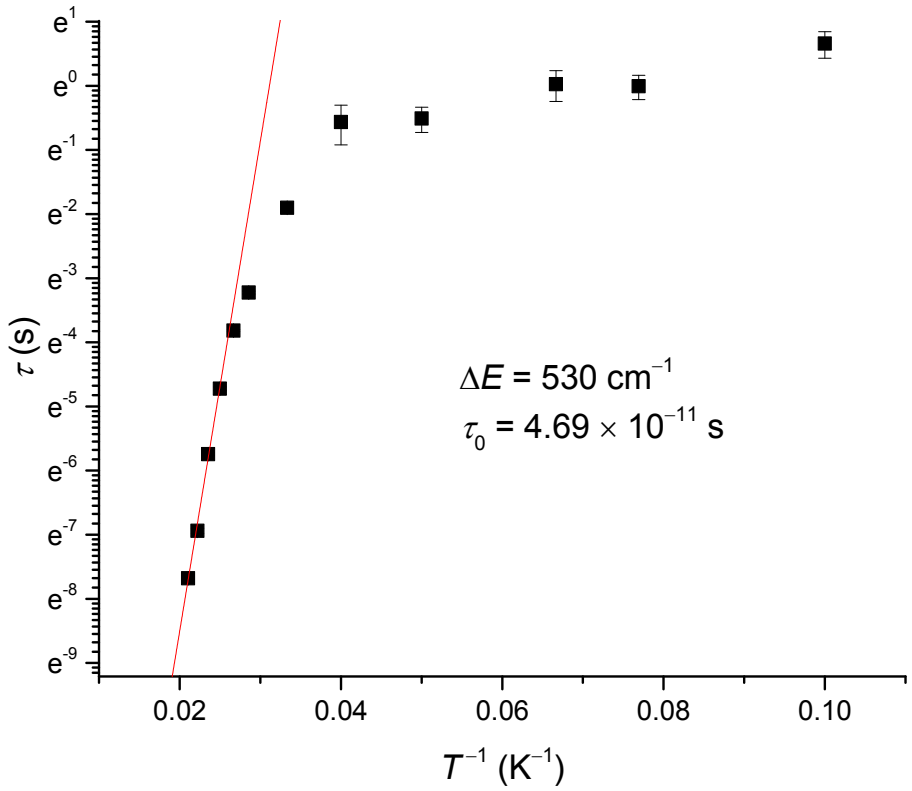

Figure S34. Arrhenius plots for $[Tb_2]^{2+}$*. Solid line was fitted by using the Arrhenius equation: $\tau = \tau_0 \exp(\Delta E/k_B T)$. Fitting the plots by using eq.1 was unsuccessful due to a large deviation in τ in the low-T region.

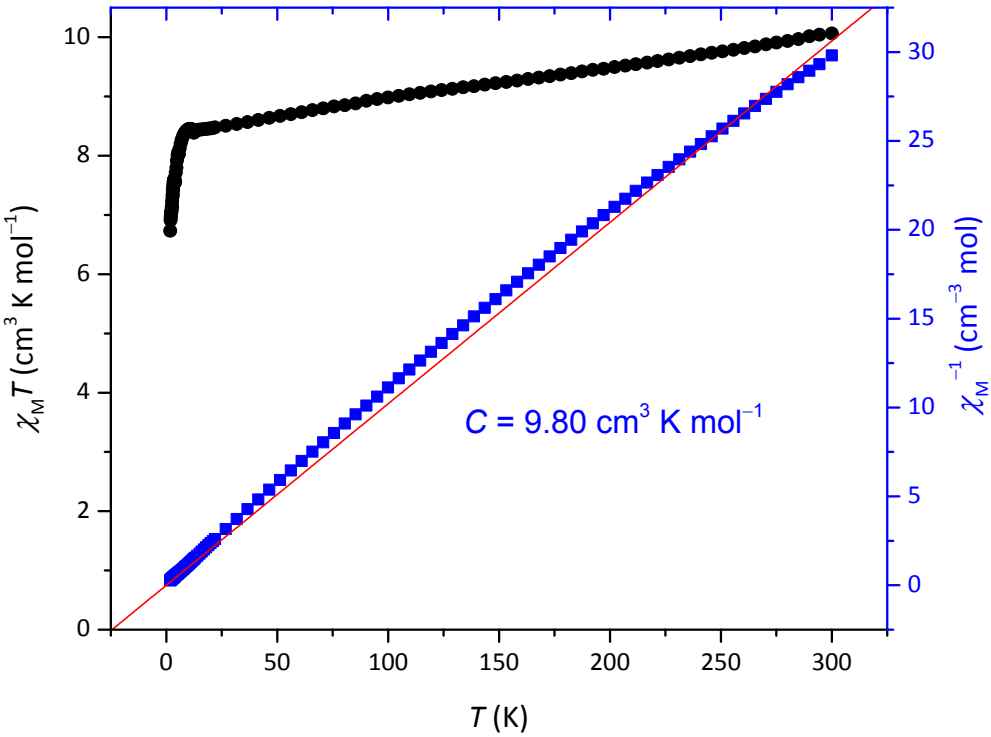

Figure S35. $\chi_M T$ vs T and χ_M^{-1} vs T plots for [Tb]$^{+}$* in a 1000 Oe dc magnetic field. Solid lines in the χ_M^{-1} vs T plots were fitted using the Curie equation for $T > 200$ K. The Curie constant is smaller than expected value (C = 11.813 cm^3 K mol^{-1} for 1 mole of Tb(III)) due to the deviation which originate from magnetic dilution.

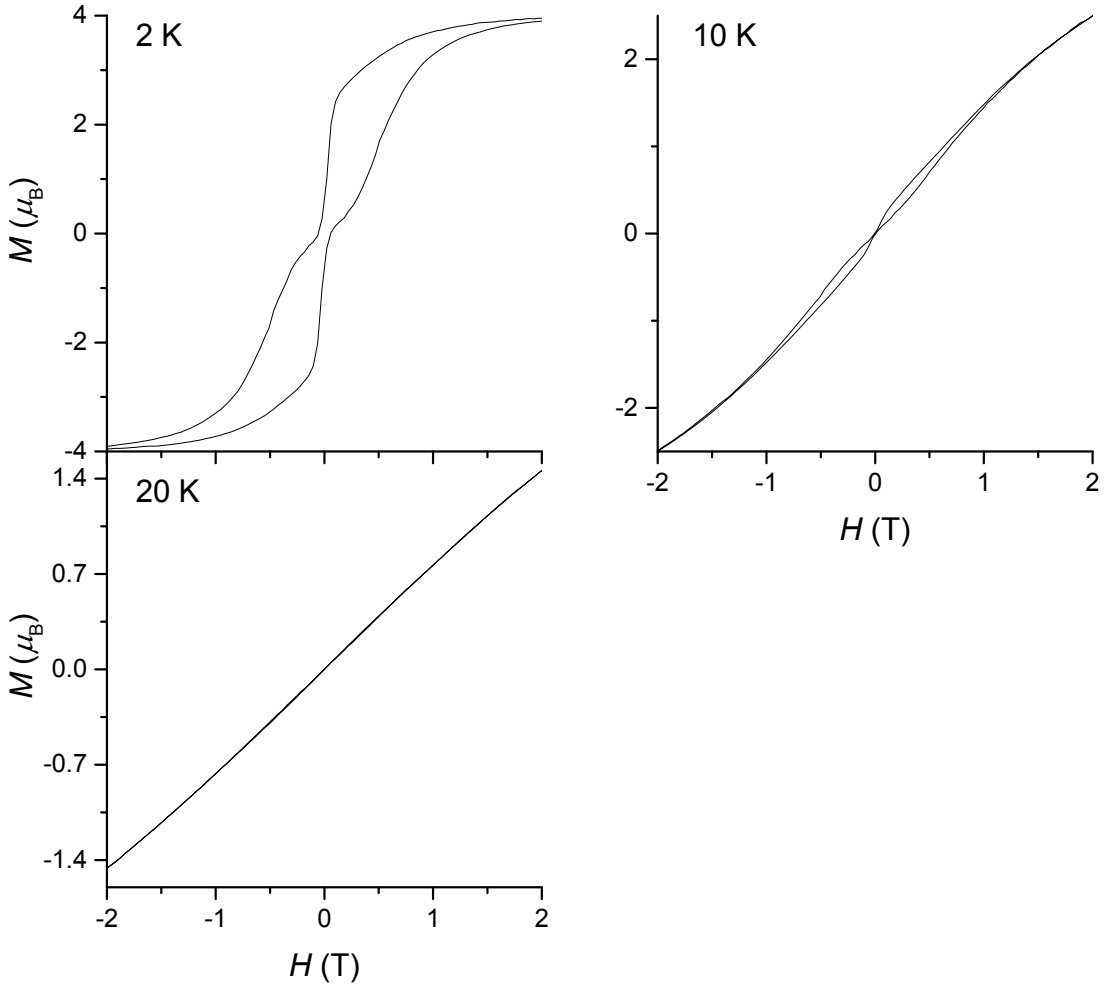

Figure S36. *MH* curves for $[Tb]^{+}$* at 2 K and a field sweep rate of 15 Oe/s.

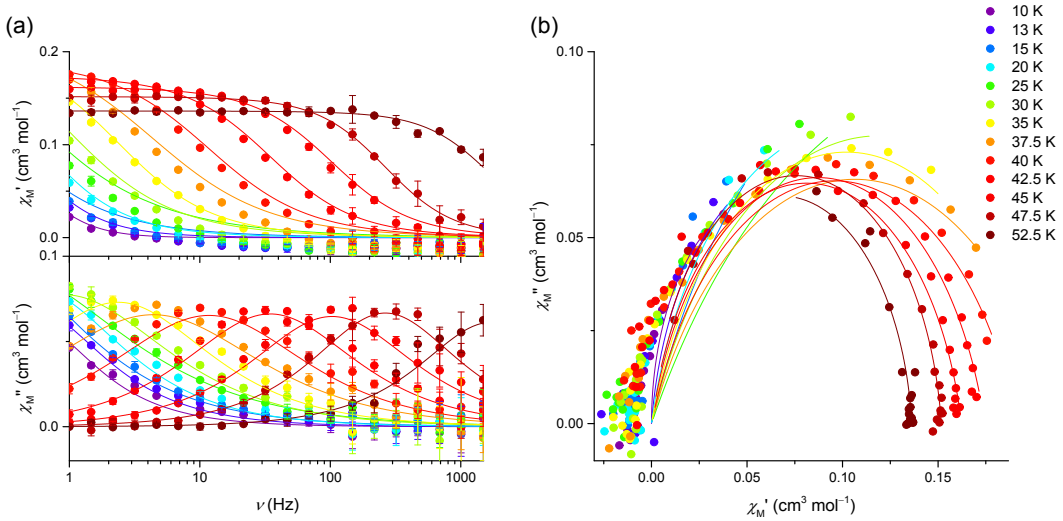

Figure S37. (a) χ_M' vs ν and χ_M'' vs ν plots (b) Cole-Cole plots for $[Tb]^{+}$* without an applied dc magnetic field. Solid lines were fitted using the Debye model.

Table S6. Fitting parameter obtained from Figure S37.

T (K)	χ_S (cm^3 mol^{-1})	dev(χ_S)	χ_T (cm^3 mol^{-1})	dev(χ_T)	τ (s)	dev(τ)	α	dev(α)
10	0	0.00187	0.12244	0.06613	0.31329	0.21377	0	0.13866
13	0	0.00237	0.16259	0.08353	0.32683	0.24793	0.09349	0.13048
15	0	0.00311	0.32655	0.33381	0.88807	1.67925	0.26693	0.13418
20	0	0.00253	0.20894	0.06757	0.28218	0.15431	0.16642	0.09191
25	0	0.0054	0.34864	0.24717	0.57052	0.95772	0.37135	0.12909
30	0	0.00329	0.2383	0.04662	0.17302	0.07053	0.26662	0.07229
35	0	0.00283	0.20426	0.01545	0.06735	0.00994	0.20987	0.04771
37.5	0	0.00461	0.21295	0.01673	0.03626	0.00675	0.29616	0.05736
40	0	0.00359	0.19139	0.00669	0.01355	0.0012	0.2378	0.03809
42.5	0	0.00281	0.17436	0.00296	0.00459	2.38127E−4	0.17355	0.02597
45	0	0.00337	0.16227	0.00212	0.00154	7.75421E−5	0.14336	0.02612
47.5	0	0.00236	0.1517	9.32205E−4	6.01633E−4	1.69583E−5	0.08185	0.01556
52.5	0	0.016	0.13623	0.0011	9.36351E−5	1.58134E−5	0.06821	0.04719

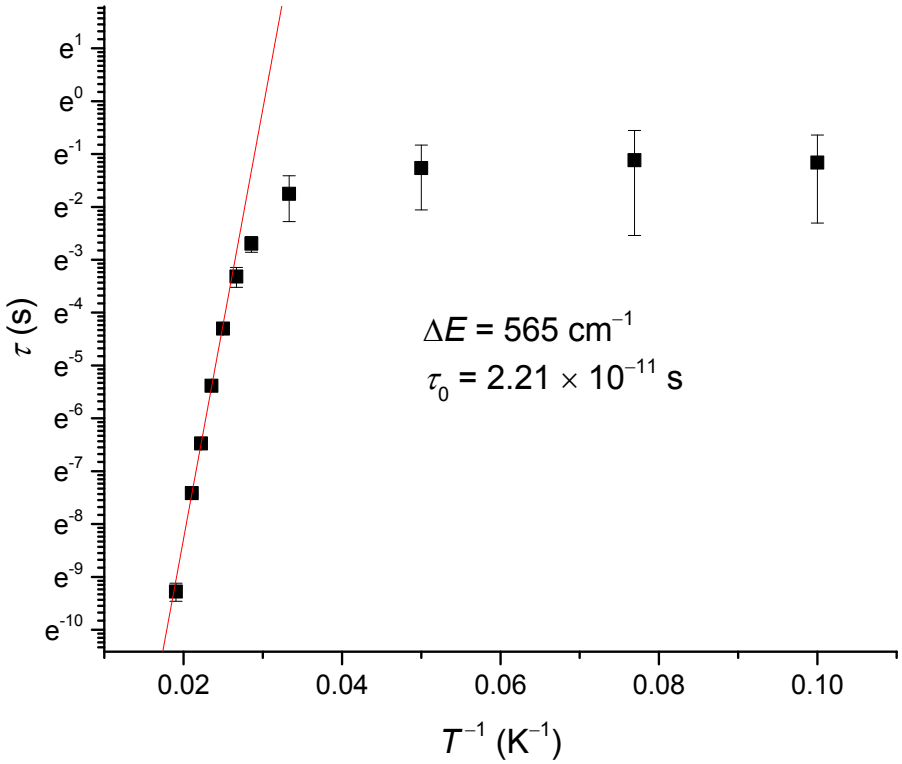

Figure S38. Arrhenius plot for $[Tb_2]^{+}$*. Solid line was fitted by using the Arrhenius equation: $\tau = \tau_0 \exp(\Delta E/k_B T)$. Fitting the plots by using eq.1 was unsuccessful due to a large deviation in τ in the low-T region.

References

1 A. Y. Tolbin, V. E. Pushkarev, L. G. Tomilova and N. S. Zefirov, *Mendeleev Commun.* **2009**, *19*, 78–80.

2 G. A. Spyroulias, C. P. Raptopoulou, D. de Montauzon, A. Mari, R. Poilblanc, A. Terzis and A. G. Coutsolelos, *Inorg. Chem.* **1999**, *38*, 1683–1696.

3 A. Y. Tolbin, V. Pushkarev, L. Tomilova and N. Zefirov, *Russ. Chem. Bull.* **2006**, *55*, 1155–1158.

4 L. Malavolti, M. Mannini, P.−E. Car, G. Campo, F. Pineider and R. Sessoli, *J. Mater. Chem. C* **2013**, *1*, 2935–2942.